Geophysical Journal International

A benchmark for finite Prandtl number convection: comparison of Boltzmann and Navier–Stokes solutions

G. Morra [1], P. Mora [2] C. Huttig [3], N. Tosi [3], H. Samuel [4] and D.A. Yuen[5]

[1]*Department of Physics, University of Louisiana at Lafayette, LA 70504, USA. E-mail: gabrielemorra@gmail.com*
[2]*College of Petroleum Engineering and Geosciences, King Fahd University of Petroleum and Minerals, Dhahran 31261, Kingdom of Saudi Arabia*
[3]*Institute of Space Research, German Aerospace Center (DLR), Berlin 12489, Germany*
[4]*Institut du Physique du Globe de Paris, CNRS, Université Paris Cité, Paris 75005, France*
[5]*Department of Applied Physics and Applied Mathematics Columbia University, New York 10027, USA*

SUMMARY

While modern thermal convection in rocky planets is controlled by a slow solid-state creep flow, the earliest stages of terrestrial planets likely experienced turbulent flow during which their silicate envelope was fully molten, usually called magma ocean. The main parameter separating the two regimes is the Prandtl number (Pr), which is so high for mantle convection to be usually assumed infinite, whereas magma oceans are characterized by Pr on the order of 1. We compared the results of isoviscous convection simulations performed with three codes: (GAIA, TLBM, StreamV). These codes are based on different numerical formulations and were used for modelling convection with Pr ranging from 1 to 1000, while exploring different convection intensity by varying the Rayleigh number (Ra) from 10^4 to 10^6. GAIA (Generic Automaton for planetary Interior Analysis) is a Finite Volume fluid flow and energy solver for the Navier–Stokes equations across arbitrary geometries. TLBM (Thermal Lattice Boltzmann Method) solves the mesoscale momentum and energy distribution densities for colliding particles on a discrete lattice. StreamV is a Eulerian–Lagrangian Finite Volume code that solves the Navier–Stokes equations under the Boussinesq approximation. The codes are compared over 24 different simulation setups, analogue to the classical Blankenbach infinite Pr benchmark, but extending it to finite Pr and to two types of boundary conditions, free-slip and no-slip. We show that the results of the three codes are generally in good agreement, and discuss differences. Finite Pr solutions show a much richer dynamics varying from stable steady-state solutions, to oscillatory and chaotic ones, and converging to infinite Prandtl number solution for increasing values of Pr for larger Ra: $Pr \geq 100$ is sufficient for $Ra = 10^5$ but $Pr \geq 1000$ is required for $Ra = 10^6$. Our results offer a robust set of solutions useful for testing future finite Prandtl number convection codes.

Key words: Numerical modelling; Numerical solutions; Heat flow; Planetary interiors; Dynamics: convection currents and mantle plumes; Physics of magma and magma bodies..

1 INTRODUCTION

Traditionally, geodynamic modelling has mainly focused on mantle convection at conditions similar to present-day Earth, characterized by infinite Prandtl number fluid dynamics because the Earth and other planetary mantles span most of their histories in solid-state convection. Recent growing interest focusing on other problems such as Archean geodynamics (van Hunen *et al.* 2008; Gunawardana *et al.* 2024), Hadean geodynamics (Marchi *et al.* 2014; Ballmer *et al.* 2017; Korenaga & Marchi 2023), convection in global-scale magma oceans on Earth (Nikolaou *et al.* 2019; Patočka *et al.* 2020; Salvador & Samuel 2023; Salvador *et al.* 2023) and on exoplanets

(Lichtenberg *et al.* 2021), as well as liquid silicate layers confined in the deepest mantle (Samuel *et al.* 2021) calls for new modelling tools that can explore this greater variety of convection regimes for terrestrial planet interiors.

Convection in an isoviscous fluid can be primarily described by two governing parameters, the Rayleigh number Ra and the Prandtl number Pr (Lohse & Shishkina 2023). Since Pr is assumed virtually infinite for mantle solid-state convection, Ra is the primary parameter used to characterize the dynamics of solid planetary interiors. For the present-day Earth's mantle, Ra is usually estimated to range between 10^5 and 10^7 (Ricard 2007), and up to 10^9 for super Earths (Valencia & O'Connell 2009; Korenaga 2010; Tackley *et al.* 2013),

numbers commonly accessible by modern computational codes. On the contrary, early hotter planetary stages are characterized by the presence of a molten silicate mantle referred to as *magma ocean* stage. During magma ocean periods, values of Pr are on the order of 1, close to values for air (Pr = 0.7) or water (Pr = 7), while Ra can reach values much larger than those associated with solid-state convecting mantle, up to $\approx 10^{30}$ (Solomatov 2007). This is well beyond the limits of what can be achieved using existing numerical modelling tools, and goes also beyond the limits of laboratory experiments (Lohse & Shishkina 2023). While our proposed benchmark is limited to Ra up to 10^6, it reaches a turbulent regime, as measured by the Reynolds number Re, which is up to Re ≈ 1000 for the lowest Pr that we consider (Pr = 1), and the codes used have been tested for Ra $\geq 10^{10}$ (Salvador & Samuel 2023; Mora *et al.* 2024).

Formally, the presence of a coefficient 1/Pr in the non-dimensional formulation of the momentum equation implies that by increasing Pr, results are expected to converge to the infinite Pr solution. We verify this observation by extending a previous benchmark for infinite Pr codes (Blankenbach *et al.* 1989a) to Pr ranging from 1 to 1000. The complexity and diversity of convection solutions that we find for Pr in the $1 - 1000$ range calls for suitable codes that optimally runs also at finite Pr, aimed at studying magma oceans and other geophysical systems such as the ocean and the atmosphere.

To our knowledge this work is the first benchmark where the same codes are tested across the spectrum that goes from 1 to virtually infinite Pr, using otherwise the same physical forcing (Ra) and boundary conditions. Previous geodynamic community benchmarks have focused on several aspects of infinite Pr dynamics (e.g., van Keken *et al.* 2008; King *et al.* 2010; Tosi *et al.* 2015a), while other finite Pr community benchmarks were proposed by different fluid dynamics communities (e.g., Nicolas *et al.* 2011; Kooij *et al.* 2018). TLBM, Thermal Lattice Boltzmann Method, was never accurately compared before with established geodynamic codes on such a wide range of parameters. The rationale for this work is therefore also to test solutions at increasing Pr values until convergence to the infinite Pr solution is reached.

The manuscript is organized as follows. Section 2 presents the initial setup, boundary conditions, and equations that are solved. Section 3 describes the methods on which the three codes rely. Section 4 illustrates the results and is divided in three parts, one focusing on a comparison of the asymptotic results, a second one on the time-dependent space-averaged velocity and on the heat flux at the top/bottom boundaries, and finally a third part on the outcome of a resolution test for the most turbulent case. In Section 5 consistencies and discrepancies between the numerical results are discussed.

2 BENCHMARK SETUP

The simulations are based on finite Pr (*i.e.* non-negligible inertia) formulation for a thermally-driven convecting fluid, heated from below and cooled from above in a 2-D square cavity with either *free-slip* or *no-slip* boundary conditions on all the four box sides. The lateral boundaries are thermally insulating, while the top and bottom surfaces are isothermal.

The equations to be solved are the momentum equation of a non-rotating Boussinesq fluid, which implies an incompressible closure, at finite Pr, which is defined as the ratio between kinematic viscosity

and thermal diffusivity

$$Pr = \nu/\kappa, \tag{1}$$

where the kinematic viscosity is the ratio between the dynamic viscosity η and the density ρ: $\nu = \eta/\rho$.

Written in non-dimensional form, and assuming a homogeneous viscosity, the momentum equations can be written as:

$$\frac{1}{Pr}\left(\frac{\partial \mathbf{u}}{\partial t} + \mathbf{u} \cdot \nabla \mathbf{u}\right) + \nabla p = \nabla^2 \mathbf{u} + Ra\, T\mathbf{e}_g, \tag{2}$$

where $\mathbf{e}_g$ is the unit vector in the direction of gravity (whose magnitude g is embedded in the Rayleigh number Ra), p is the dynamic pressure, T is the temperature normalized by the total temperature contrast ΔT between the two horizontal surfaces and therefore ranges between 0 and 1. The Rayleigh number measures the intensity of the convective vigor, physically defined by the ratio between the thermal buoyancy and the resisting effects due to the momentum and thermal diffusion. In a Cartesian domain of height D, Ra is expressed as:

$$Ra = \frac{\alpha g \Delta T D^3}{\nu \kappa}, \tag{3}$$

where g is the gravitational acceleration and α is the thermal expansion.

The momentum equation is closed with the incompressible equation, representing the conservation of mass in the Boussinesq approximation:

$$\nabla \cdot \mathbf{u} = 0, \tag{4}$$

coupled to the energy conservation equation for a non-dimensional temperature T:

$$\frac{\partial T}{\partial t} + \nabla \cdot (\mathbf{u}T) = \nabla^2 T, \tag{5}$$

where the second term can be equally expressed as $\mathbf{u} \cdot \nabla T$ due to incompressibility $\nabla \cdot \mathbf{u} = 0$. The setup with the initial conditions is shown in Fig. 1. Two of the codes (GAIA and StreamV) use a different space and time rescaling from TLBM, due to different solving strategies, therefore the results are shown as a function of dimensionless time using diffusion time scale (D^2/κ). Similarly, the velocity is rescaled as κ/D. The temperature is renormalized to ΔT, the difference between top and bottom temperatures in the domain considered.

GAIA simulations were conducted with a resolution of 150×150 and solution-dependent time stepping. All TLBM simulations used a resolution of 512×512 and 10^7 time steps, except for Ra = 10^6 and Pr = 1000 for which the number of time steps were increased up to 10^8 to obtain convergence to infinite Pr. StreamV results were obtained on a grid consisting of 64×64 square cells for all cases except for Ra = 10^6 and Pr = 1 where a grid of 128×128 was used to warrant a sufficiently accurate solution.

2.1 Boundary and initial conditions

We tested two types of boundary conditions (BCs), in both cases adopted on all four sides of the model domain: either *free-slip* (as in Blankenbach *et al.* 1989a) or *no-slip* (also called *rigid* or *fixed*). The temperature is constant at the top ($T = 0$) and at the bottom ($T = 1$), and the heat flux is zero on the sidewalls. Since physical parameters are assumed to be homogeneous in the entire domain, the dynamics depends only on Pr and Ra, besides initial and boundary conditions.
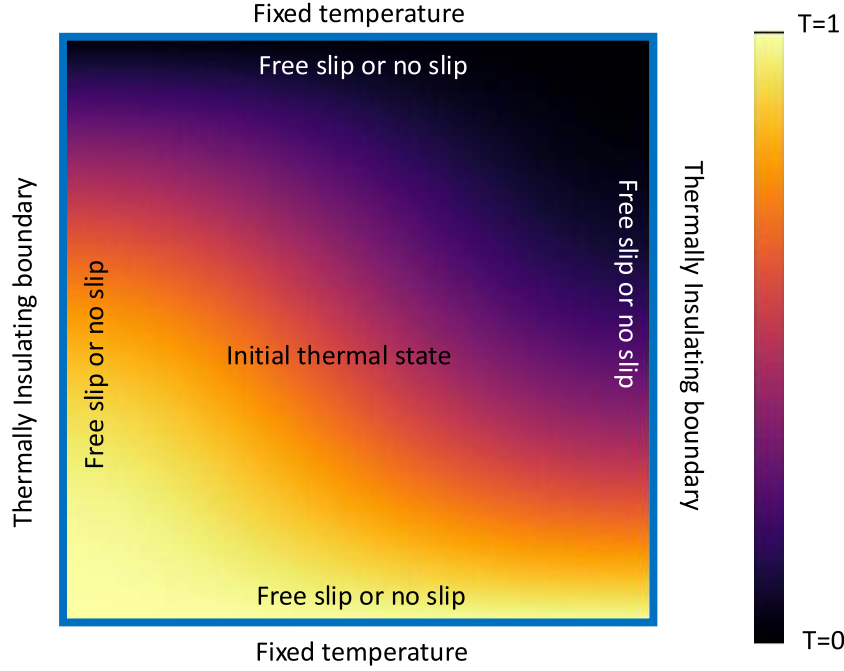
Figure 1. Setup of the benchmark. The field represents the initial temperature field. The horizontal (x) and vertical (z) coordinates are assumed to be from 0 to 1.

The initial condition for the velocity is zero everywhere, while we adopt an initial choice for T that forces convection in one direction, otherwise different symmetric solutions can emerge:

$$T(x, z, t = 0) = [z + 0.3 \sin(\pi z) \cos(\pi x)], \tag{6}$$

where x is the horizontal coordinate and z is depth, both of them going from zero to one. We observed that while for the free-slip BC the initial condition does not influence the long-term solution (*e.g.* stationary or chaotic), for the *no-slip* cases different initial conditions trigger different final solutions. For example, the oscillatory solution that we observe at $Ra = 10^5$ and $Pr = 100$ appears only with certain initial conditions such as the one chosen here.

Each simulation runs for a dimensionless time $t_{max} = 0.35$. Models with $Ra = 10^4$ rapidly reach steady-state, while for higher Ra oscillatory solutions can develop (for certain values of Pr and *no-slip* boundary conditions), or even remain in a permanent chaotic regime where a steady solution is never reached.

2.2 Metrics used to compare models

We primarily resort to values summarizing the results of each simulation through time. In particular, similarly to previous analogous benchmarks, we calculate (1) the root mean square of the velocity V_{rms}, a way of averaging the velocity magnitudes across the entire domain, taking into account both the horizontal and vertical components of the flow, and (2) the Nusselt number Nu, defined as:

$$V_{rms} = \left[\int_0^1 \int_0^1 (u_x^2 + u_z^2) \, \mathrm{d}x \, \mathrm{d}z \right]^{1/2} \tag{7}$$

$$Nu = \frac{1}{\Delta T} \int_0^1 \left. \frac{\partial T(x, z)}{\partial z} \right|_{z=1} \mathrm{d}x, \tag{8}$$

where the velocities are renormalized by D/κ and it is assumed that $\Delta z = \Delta x = 1$ and $\Delta T = 1$ is the difference between the bottom and the top temperatures. If the model does not reach steady-state,

we compute the average value between dimensionless times 0.25 and 0.35.

We compared the root mean square velocity (V_{rms}) and the Nusselt number (Nu) for all the 24 tested setups (3 Ra cases × 4 Pr cases × 2 BCs). We compared the averaged temperature (T_{ave}) for all models, but we do not show here the results as they are not insightful because of the problem symmetry (see eq. 6 and Fig. 1) leading to T_{ave} close to 0.5 for most cases. Simulations with `GAIA` were performed by C. Huttig, while `StreamV` simulations were conducted by H. Samuel. V_{rms} and Nu were extracted by G. Morra and represented as time-series in a homogeneous format. While the results for the low Ra numbers ($Ra = 10^4$ and $Ra = 10^5$) are sufficiently smooth to be clear at any sampling, the chaotic results for $Ra = 10^6$ and $Pr \geq 10$ diverge in the details. For this reason, we sampled a range of 1000 to 2000 points to show how the solution varies without cluttering the image. Finally V_{rms} and Nu have been tabulated, choosing the steady-state value when existing, or computing the time average from $t = 0.25$ to $t = 0.35$ elapsed time.

3 CODES USED

We describe here three software packages developed for modelling fluid-dynamics solving the momentum (Navier–Stokes Equations, hereafter NSE) and energy equations (`StreamV` and `GAIA`) or to solve the mesoscale Boltzmann equation which asymptotically converges to the solution of the thermal NSE (`TLBM`).

3.1 GAIA software

The development of the Generic Automaton for planetary Interior Analysis (`GAIA`) began in 2006 at the German Aerospace Center (DLR), Institute of Planetary Research in Berlin. `GAIA` is written in C++ and has no external dependencies, making it self-contained too, except for the possibility to additionally use external linear solvers.

GAIA is a fluid flow and energy solver for the incompressible and compressible (anelastic) Navier–Stokes equations across arbitrary 2-D and 3-D geometries. Initially designed to simulate Stokes flow (creeping flow) with strongly varying viscosity (Hüttig *et al.* 2013), GAIA has since been extended to support flows driven by inertia. Also supporting a wide range of geometries, these advanced features make GAIA an ideal tool for simulating a variety of geophysical flows such as mantle, core, and ocean convection.

GAIA was initially designed to operate in a 3-D spherical shell using a spiral grid (Hüttig & Stemmer 2008b). The conservation equations are solved using the Finite-Volume Method applied to Voronoi cells (Hüttig & Stemmer 2008a). Classical domain decomposition with Message Passing Interface is employed for massively parallel computations, allowing GAIA to handle large and complex datasets. For the advection scheme, GAIA utilizes a flux limiter (van Leer 1979), which is second-order accurate in smooth flow regions, and a third-order implicit time integration scheme. The implicit time stepping helps to overcome the Courant criterion, enabling less restrictive time steps. In the presence of uniform grids such as those used in this benchmark, the co-located arrangement of temperature and velocity fields at cell centers renders the solution of the Stokes and diffusion equations also second-order accurate. The momentum matrix is not split, solving the momentum and mass conservation equations for velocities and pressure in the same step. Energy conservation is solved in a separate step, including nonlinear iterations if necessary (Picard iterations).

GAIA offers flexibility in solver selection, ranging from direct solvers such as MUMPS (MUltifrontal Massively Parallel sparse direct Solver, Amestoy *et al.* 2001, 2006) for small problems to a variety of iterative solvers for larger problems. Parallel GPU support is also enabled via the CUDA (Compute Unified Device Architecture) interface, even in hybrid GPU/CPU setups.

Over the years GAIA has been validated through a variety of benchmark tests for thermal convection in 2-D rectangular geometries, including incompressible and compressible flow with infinite Prandlt number and temperature-dependent viscosity (Blankenbach *et al.* 1989a; King *et al.* 2010), as well as strain-rate-dependent viscosity (Tosi *et al.* 2015b), and incompressible flow with finite Prandlt number (Erturk *et al.* 2005). In addition, GAIA has been extensively tested for thermal convection in curvilinear geometries, including 2-D cylinders and spherical annuli (Fleury *et al.* 2024) and 3-D spherical shells (Christensen *et al.* 2001; Zhong *et al.* 2008).

The Nusselt number at the top of the domain (eq. 7) is computed from the uppermost gradient of the laterally averaged temperature field by finite difference. In practice, the first cell value below the boundary is subtracted from the boundary value (*i.e.* zero at $z = 1$) and divided by half the vertical cell size. The RMS velocity eq. (8) is simply computed using the co-located components of the solution at cell centers.

3.2 StreamV software

StreamV is a Eulerian–Lagrangian parallel Finite Volume code written in Fortran that solves the Navier–Stokes equations under the Boussinesq approximation coupled to the conservation of energy and/or composition, at either infinite or finite Prandtl numbers in 2-D and 3-D Cartesian or curvilinear geometries.

In plane geometries, the code can rely on a primitive variable formulation, or on a pure stream function formulation that satisfies automatically the conservation of mass. Both formulations have been benchmarked against various numerical and analytical

solutions (Samuel & Evonuk 2010; Samuel 2012, 2018; Tosi *et al.* 2015b; Salvador & Samuel 2023), and as pointed out in previous studies (Blankenbach *et al.* 1989b; van Keken *et al.* 1997; Deubelbeiss & Kaus 2008; Tosi *et al.* 2015b), yield very similar results. Here, results are obtained using the pure stream function formulation as an alternative to the primitive variable formulation used in GAIA. For 2-D geometries and in the presence of inertial terms, the stream function formulation reduces the three Navier–Stokes equations (x- and z-momentum and the continuity equation) to a single scalar parabolic equation for the stream function, ψ. The latter relates to the velocity vector components as: $\mathbf{u} = (u_x, u_z) = (\partial \psi / \partial z, -\partial \psi / \partial x)$. The governing scalar equation is obtained by taking the curl of the momentum equations and substituting the velocity vector components using the definition of the stream function. In the case of constant viscosity considered here, this leads to the following dimensionless equation:

$$\frac{D\nabla^2 \psi}{Dt} = \nabla^2(\nabla^2 \psi) - \mathrm{Ra}\frac{\partial T}{\partial x}, \qquad (9)$$

where $DX/Dt = \partial_t X + \mathbf{u} \cdot \nabla X$ expresses the Lagrangian derivative of the scalar quantity X. Expanding the Lagrangian derivative and making use of the definition of the stream function, the above equation can be written as:

$$\frac{\partial \nabla^2 \psi}{\partial t} = \nabla^2(\nabla^2 \psi) - \mathbf{u} \cdot \nabla(\nabla^2 \psi) - \mathrm{Ra}\frac{\partial T}{\partial x}, \qquad (10)$$

where spatial derivatives are discretized on a staggered grid in which ψ is defined at nodal (co-located) points, leading to velocity vector components defined at the center of each cell surface, while the temperature is defined at cell centers. Relying on such staggered grid allows one to approximate first-order derivatives in each direction with finite differences of second-order accuracy involving only two adjacent points. This corresponds to 13-points finite difference stencils due to the fourth-order derivatives involved. Recognizing that $\nabla^2 \psi$ is the vorticity ω, the second term on the right-hand side of eq. (10) corresponds to the advection of ω along the flow streamlines, and is handled via a nonlinear upwind biased scheme using a *minmod* limiter (Kupferman 2001), which is of second-order accuracy for a sufficiently smooth field. The left-hand side of eq. (10) is approximated by an explicit scheme between two consecutive time steps t and $t + \Delta t$:

$$\nabla^2 \psi(t + \Delta t) = \nabla^2 \psi(t) + \Delta t$$
$$\left\{ \nabla^2[\nabla^2 \psi(t)] - \mathbf{u}(t) \cdot \nabla[\nabla^2 \psi(t)] - \mathrm{Ra}\frac{\partial T(t)}{\partial x} \right\}, \qquad (11)$$

where the time step Δt is subject to the following stability criteria involving the Prandtl number and the minimum grid spacing, Δh: $\Delta t \leq \Delta h^2/(4\,\mathrm{Pr})$. The resulting Poisson eq. (11) is solved for $\psi(t + \Delta t)$ using a geometric multigrid approach (Brandt 1977), performing V-cycles with a Jacobi smoother. *Free slip* ($\partial^2 \psi / \partial n^2 = 0$, where n indicates the normal to the boundary) and *no-slip* boundary ($\partial \psi / \partial n = 0$) conditions for ψ are enforced via one layer of ghost nodal points, together with the requirement that $\psi = 0$ along all domain boundaries (Houston & De Bremaecker 1974), while Dirichlet and Neumann temperature boundary conditions are enforced using a layer of ghost cell points along each boundary (Patankar 1980). This numerical scheme for solving the Navier–Stokes equations without the buoyancy term was also successfully benchmarked against numerical solutions at various Prandtl numbers following the lid-driven cavity benchmark (Ghia *et al.* 1982).

Temperature is advected using a fifth-order upwind-biased scheme (Jiang & Shu 1996) (subject to a less restrictive Courant

stability criterion than that of the bi-harmonic equation) applied to each direction separately that results in small numerical diffusion (Samuel 2014).

The time-dependent biharmonic eq. (11) and conservation of energy are integrated in time with an explicit second-order, Total Variation Diminishing Runge–Kutta Scheme (Harten 1983).

The fifth-order discretization for advection terms with second-order for other spatial derivatives in `StreamV`, along with the use of the staggered grid where the stream function is defined at collocated nodes (as discussed above), yields a formal second-order spatial accuracy. Note that for a specific case, we also used `StreamV` with a primitive variable formulation where the pressure and velocities are solved using a projection method (Chorin 1968) leading to a pressure Poisson equation that is solved using a geometric multigrid method.

For `StreamV` the temperature gradient that enters the Nusselt number was computed by finite differences using the cell-centered values located just above and below $z = 1$, leading to a second-order precision in space. These values were then horizontally averaged using an arithmetic mean. RMS velocities were computed at collocated grid points. When the stream function formulation is used the u_x and u_z components were computed from the values of the stream function (defined at co-located locations) using a second-order centered scheme. For the cases where the primitive variable formulation was used u_x and u_z at collocated nodes were computed by arithmetic averaging of the closest velocity components defined at cell center surfaces, which also yields second-order accuracy.

3.3 TLBM: Thermal Lattice Boltzmann Method

The Lattice Boltzmann Method (LBM) is an alternative approach to classical numerical solutions to PDE's for modelling fluid dynamics, such as the other two codes used for this benchmark, and it is based on simulating the Boltzmann Equation on a discrete lattice Chen & Doolen (1998). In this approach, particle number densities carrying mass are moved on a discrete lattice with collisions being achieved by relaxing the number densities towards the Boltzmann equilibrium distribution Bhatnagar *et al.* (1954). Historically, the LBM has been applied to simulating many fluid dynamics problems Succi & Succi (2018) including multiphase flow in porous media Huang *et al.* (2015); Mora *et al.* (2021), plastic flows Leonardi *et al.* (2015) and magnetohydrodynamics Dellar (2002). In the implementation used here, the solution of the energy equation is added to the standard LBM using a second number density carrying energy density. The buoyancy forcing associated to thermal expansion is implemented through a Boussinesq term Peng *et al.* (2003). An early version of the code used for this benchmark has been used to study Rayleigh number flow in the range Pr $\in [1, 5 \times 10\,000]$ and Ra $\in [1708, 10^{10}]$ Mora & Yuen (2018). Recent efforts have shown how nonlinear rheology can be implemented and used to model spontaneous emergence of plate tectonics from mantle convection Mora *et al.* (2024), multiphase LBM Mora *et al.* (2021) applied to planetary accretion simulations Honarbakhsh *et al.* (2025) and combined with machine learning to extract model parameters from simulation snapshots Ali Boroumand *et al.* (2024). In a recent yet unpublished implementation, convection at a record Ra $= 10^{15}$ has been achieved Mora *et al.* (2023).

The Thermal Lattice Boltzmann Method (TLBM) moves and collides two distributions f_α and g_α representing a fluid's mass and energy density where α is the movement direction on a discrete 2-D or 3-D lattice. This is achieved in two steps of movement (or streaming) and collision where collision is achieved by relaxing the relevant distribution towards the Boltzmann equilibrium distribution. These two steps applied to f_α yield the incompressible Navier–Stokes equations (Chen & Doolen 1998), and the two steps applied to g_α yield the convection-diffusion equation describing energy density conservation (Krüger *et al.* 2017). The addition of a Boussinesq buoyancy forcing term to the mass density f_α leads to the equations for thermal convection.

The streaming step can be written as

$$f_\alpha(\mathbf{x}, t) = f_\alpha(\mathbf{x} - \mathbf{c}_\alpha \Delta t, t - \Delta t) \quad , \tag{12}$$

and

$$g_\alpha(\mathbf{x}, t) = g_\alpha(\mathbf{x} - \mathbf{c}_\alpha \Delta t, t - \Delta t) \quad , \tag{13}$$

where the time step is $\Delta t = 1$ lattice time units and $\mathbf{c}_\alpha$ is the velocity vector which points to adjacent lattice sites along axes or diagonally on planes. Hence, $\mathbf{c}_\alpha \Delta t = \mathbf{c}_\alpha$ equals one lattice spacing orthogonally or diagonally in a square or cubic unitary lattice with $\Delta x = 1$. As such, $|\mathbf{c}_\alpha \Delta t| = \Delta x$ for the α's representing orthogonal directions and $|\mathbf{c}_\alpha \Delta t| = \sqrt{2}\Delta x$ for the α's along the diagonals of each 2-D plane.

The macroscopic properties, density ρ, velocity $\mathbf{u}$ and energy density ε relate to the number densities via

$$\rho = \sum_\alpha f_\alpha \quad , \tag{14}$$

$$\mathbf{u} = (1/\rho) \sum_\alpha f_\alpha \mathbf{c}_\alpha \quad , \tag{15}$$

and

$$\varepsilon = (1/\rho) \sum_\alpha g_\alpha \quad , \tag{16}$$

where the energy density ε relates to temperature through $T = (2/(DR))\varepsilon$ where D is the number of dimensions and R is the gas constant which is set to unity for the usual non-dimensional TLBM simulations.

The collision step including the Boussinesq buoyancy forcing term can be written as

$$f_\alpha^*(\mathbf{x}, t) = f_\alpha(\mathbf{x}, t) + \Delta f_\alpha^C(\mathbf{x}, t) + F^B(\mathbf{x}, t) \quad , \tag{17}$$

and

$$g_\alpha^*(\mathbf{x}, t) = g_\alpha(\mathbf{x}, t) + \Delta g_\alpha^C(\mathbf{x}, t) \quad , \tag{18}$$

where superscript * indicates that the distributions are post collision, F^B is the Boussinesq buoyancy forcing term, and Δf_α^C and Δg_α^C are the collision terms. These collision terms can be calculated by relaxing the distributions f_α and g_α towards their equilibrium distributions (Bhatnagar *et al.* 1954) using

$$\Delta f_\alpha^C = (f_\alpha^{eq} - f_\alpha)/\tau_f \quad , \tag{19}$$

$$\Delta g_\alpha^C = (g_\alpha^{eq} - g_\alpha)/\tau_g \quad , \tag{20}$$

where τ_f and τ_g are relaxation times, which relate to kinematic viscosity ν and thermal diffusivity κ through

$$\tau_f = \frac{\nu}{c_s^2 \Delta t} + 0.5 = 3\nu + 0.5 \quad ,$$

and

$$\tau_g = \frac{\kappa}{c_s^2 \Delta t} + 0.5 = 3\kappa + 0.5 \quad ,$$

where $c_s = 1/\sqrt{3}$ is the acoustic wave speed in the lattice. The distributions f_α^{eq} and g_α^{eq} are the equilibrium distributions for f_α

and g_α which can be calculated via a second order Taylor expansion of the Boltzmann equilibrium distribution as

$$f_\alpha^{\text{eq}} = \rho w_\alpha \left(1 + \frac{\mathbf{c}_\alpha \cdot \mathbf{u}}{c_{\text{s}}^2} + \frac{1}{2} \frac{(\mathbf{c}_\alpha \cdot \mathbf{u})^2}{c_{\text{s}}^4} - \frac{1}{2} \frac{\mathbf{u}^2}{c_{\text{s}}^2} \right) \ ,$$

$$= \rho w_\alpha \left(1 + 3(\mathbf{c}_\alpha \cdot \mathbf{u}) + \frac{9}{2}(\mathbf{c}_\alpha \cdot \mathbf{u})^2 - \frac{3}{2}\mathbf{u}^2 \right) \ , \quad (21)$$

and

$$g_\alpha^{\text{eq}} = \varepsilon f_\alpha^{\text{eq}} \ , \quad (22)$$

where w_α are the lattice weights which sum to unity and differ in 2-D and 3-D. These will be detailed in the following subsections.

The Boussinesq buoyancy forcing term F^{B} is given by

$$F_\alpha^{\text{B}} = -3 w_\alpha \rho \beta \delta T \mathbf{c}_\alpha \cdot \mathbf{g} \ , \quad (23)$$

where β is the thermal expansion coefficient, δT is the temperature perturbation and $\mathbf{g}$ is the acceleration due to gravity.

While the above equations are correct for both 2-D and 3-D setups, weight vectors w_α and velocity vectors $\mathbf{c}_\alpha$ are different in 2-D and 3-D, as they depend on the lattice dimensions and structure. The standard TLBM DdQq notation is used here where d is the number of dimensions in space, and q is the number of velocity vectors used for the lattice. All TLBM simulations in this benchmark use a D2Q9 lattice ($d = 2$ dimensional, $q = 9$ velocity vectors) whose weights are:

$$w_\alpha = (w_0, w_1, w_1, w_1, w_1, w_2, w_2, w_2, w_2) \quad (24)$$

where $w_0 = 4/9, w_1 = 1/9$ and $w_2 = 1/36$, and the velocity vectors are

$$\mathbf{c}_\alpha = \begin{matrix} [(0, 0), \\ (1, 0), (0, 1), (-1, 0), (0, -1), \\ (1, 1), (-1, 1), (-1, -1), (1, -1)] \end{matrix} \quad . \quad (25)$$

For TLBM the Nusselt number was calculated using the temperature gradient by finite differences of the second and third cells above the boundary, and by horizontally averaging the gradient with an arithmetic mean. RMS velocities were calculated as the square root of the average of the square of the velocity magnitude for each cell of the computing domain.

4 RESULTS

We analyze the results in three steps. First we quantitatively compare the asymptotic time and space averaged values for each simulation, and compare them with the infinite Pr solution for *free slip* boundary conditions. Second, we look at the space-averages of V_{rms} and Nu through time, which show that long-term solutions can be steady, oscillatory, or chaotic. This analysis is more qualitative, since differences between the results of the different codes can be of several types, in some cases in the initial transient phase, in others with the emergence of a time-shift, for example for periodic solutions, in others still these differences emerge towards the asymptotic phase. Finally, in a final subsection, we discuss the results of a resolution test for the most turbulent case, Ra = 10^6 and Pr = 1.

Prior to diving into the time-dependent solutions, we show in Figs 2 and 3 the final step of the T and V_{rms} fields for all the simulations tested from TLBM results, to illustrate the variety of fields obtained. Some of these solutions are steady-state, others are just one snapshot in time of a transient field.

4.1 Asymptotic solutions

Similarly to previous benchmarks, we aim at comparing the average V_{rms} and Nu at steady-state, if it exists. V_{rms} and Nu are calculated as the average between elapsed times $t = 0.25$ and $t = 0.35$. The 72 solutions, obtained with the three codes for each of the 24 benchmarks, are summarized in two tables, one for the 12 benchmarks with *no-slip* BCs (Table 1) and the other 12 for *free slip* BCs (Table 2).

Since the benchmark was initially designed as an extension of the Blankenbach test (Blankenbach *et al.* 1989a), we can compare the solutions with *free slip* BCs with the infinite Pr number solutions emerging from that collective effort. It is expected that for a sufficiently high Pr the solution will converge to the infinite Pr solution, therefore the Blankenbach results are placed in two special columns in Table 2, one column for the tabulated V_{rms} and one for Nu.

For the *no-slip* case, no benchmarks are available in the literature, therefore we compare the three solutions (Table 1). Differences appear between the codes, generally of 1 per cent or less, but occasionally for the most turbulent cases, up to 10 per cent for Nu. Several hypotheses are possible to justify the observed dissimilarities. They might be related to the different implementation of the *no-slip* BCs in the different numerical approaches, as well as the required resolution close the boundary of each implementation. Here the main results in more detail:

(i) For Ra = 10^4, regardless of Pr the discrepancies between steady-state V_{rms} solutions are small, the largest being between GAIA and StreamV for Pr = 1, where the two solutions differ by less than 1 per cent. For Pr = 1000, the largest discrepancy, between TLBM and StreamV is 0.5 per cent. The Nu values are also consistent, but TLBM displays systematically smaller values than the other two codes, by about 1 per cent for Pr up to 100, but increasing for larger Pr up to $\approx$ 5 per cent for Pr = 1000. This anomaly is discussed in Section 5.

(ii) For Ra = 10^5 the code discrepancies in both V_{rms} and Nu are also within 1 per cent for Pr = 1 and Pr = 10. Interestingly, for Pr = 100 and Pr = 1000, when the stable oscillatory solution arises, and averages are affected by the shift of oscillations between different solutions, V_{rms} discrepancies remain below 3 per cent and *Nu* below 2 per cent across all codes.

(iii) For Ra = 10^6 larger differences are to be expected, since chaotic solutions appear diverse in the time-dependent plots (Fig. 8). Interestingly, the largest differences are not seen in V_{rms} whose values are generally within 5 per cent from each other, but increase for Nu for which the three codes predict values that differ up to 10 per cent for Pr = 1 and for Pr = 1000.

Free slip solutions show a high degree of coherence. In particular:

(i) For Ra = 10^4, Nu for the three codes remains within 1 per cent from each other, however differences appear for Pr = 1, where GAIA displays lower V_{rms} of about 3 per cent compared to the other codes. For increasing Pr, both GAIA and StreamV converge towards the Blankenbach benchmark results, and for Pr = 1000 discrepancies remain within the order of 0.1 per cent while TLBM V_{rms} differs from the other codes by $\approx$ 1 per cent, and by $\approx$ 0.2 per cent for Nu.

(ii) For Ra = 10^5, only differences on the order of 1 per cent in V_{rms} and 0.5 per cent for Nu between the codes appear for Pr = 1. These differences remain of the same magnitude with increasing Pr and substantially all codes converge to the Blankenbach benchmark for Pr = 1000, with the largest discrepancy being for TLBM V_{rms} which is however only of about 1 per cent.

(iii) Results for Ra = 10^6 are more complex, showing substantial differences. In general, while for lower Ra asymptotic
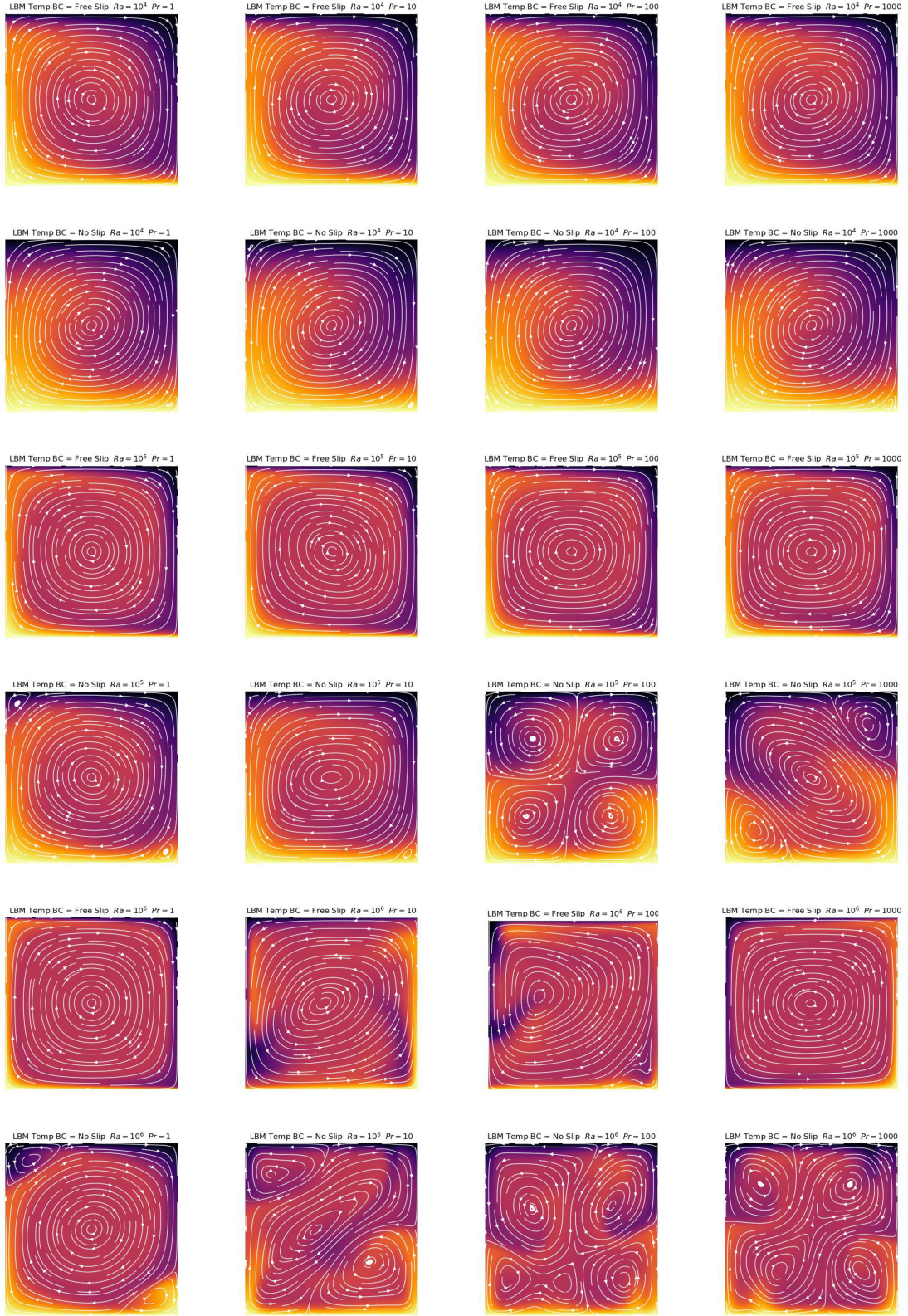
Figure 2. Last step ($t = 0.35$) of the Temperature solutions for the 24 tests performed in this work, as obtained by the TLBM code. The top three rows and the left column represent steady-state solutions, while the others capture only a transient outcome. The colourbars are not shown, as they all go from 0 to 1.
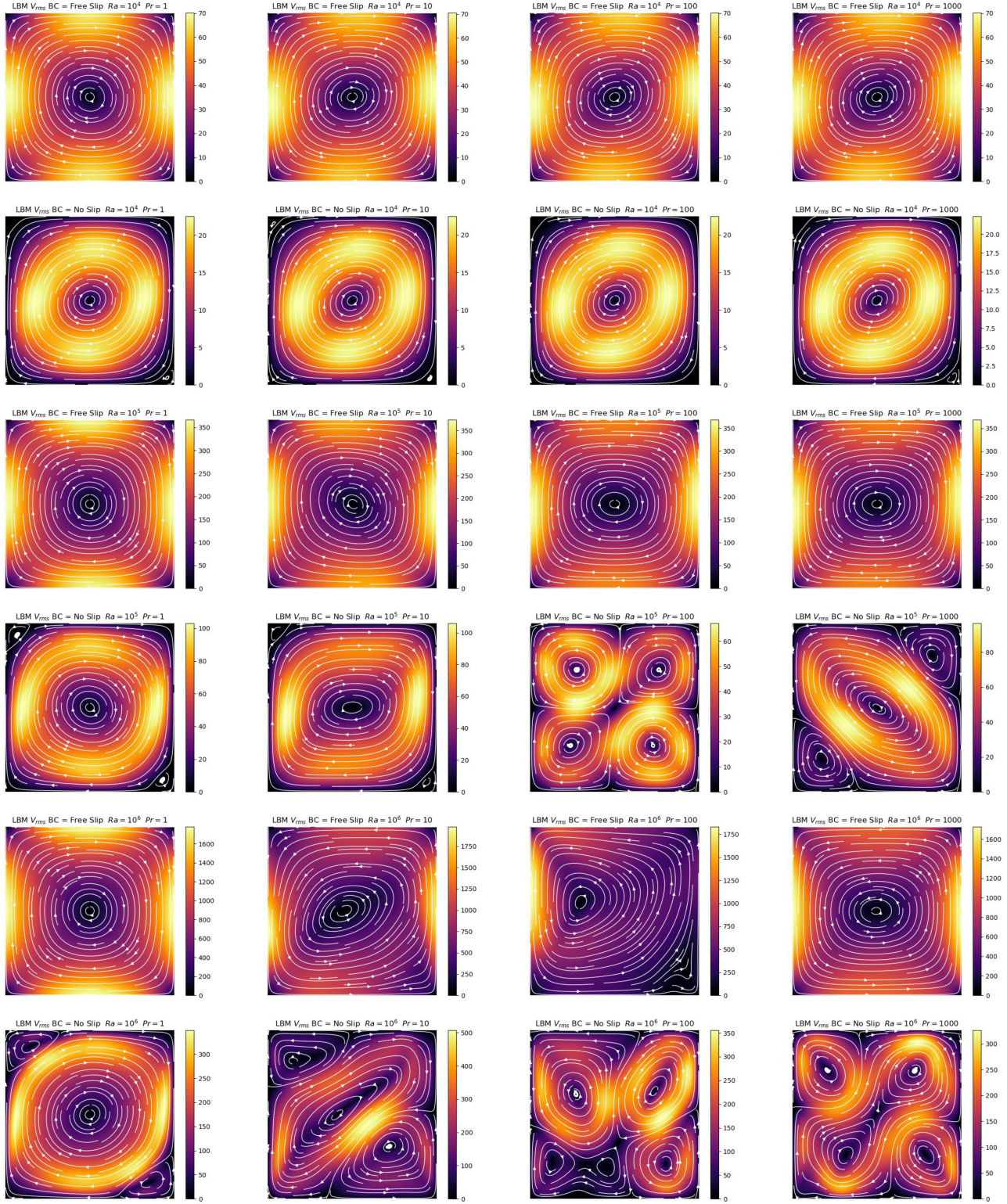
Figure 3. Last step ($t = 0.35$) of the V_{rms} solutions for the 24 tests performed in this work, as obtained by the TLBM code. The top three rows and the left column represent steady-state solutions, while the others capture only a transient behaviour.

values of V_{rms} and Nu are almost identical between $\mathrm{Pr} = 100$ and $\mathrm{Pr} = 1000$, differences between the three codes solutions of over 10 per cent appear for the more chaotic $\mathrm{Ra} = 10^6$. As for lower Ra values, all three codes converge towards the Blankenbach solution for $\mathrm{Pr} = 1000$, however TLBM and StreamV

decrease from larger values while GAIA increase from lower values. As for the other Ra cases, TLBM asymptotic values are more distant from the Blankenbach benchmark compared to the other codes, this time by ≈ 2 per cent for V_{rms} and ≈ 8 per cent for Nu.

Table 1. Asymptotic results for the 12 models with *no-slip* boundary conditions. Each value is calculated as the average of either $V_{\rm rms}$ or Nu from elapsed time 0.25 to 0.35. For some of the values this is the asymptotic steady results, while for others it is the average of either an oscillating or chaotic evolution.

Ra	Pr	$V_{\rm rms}$ $(GAIA)$	$V_{\rm rms}$ $(TLBM)$	$V_{\rm rms}$ (StreamV)	Nu (GAIA)	Nu (TLBM)	Nu (StreamV)
10^4	1	14.1582	14.2523	14.2695	2.1658	2.1503	2.1685
10^4	10	14.3537	14.3748	14.3834	2.1935	2.1761	2.1937
10^4	100	14.3796	14.4015	14.4013	2.1971	2.1776	2.1970
10^4	1000	14.3823	14.3335	14.4031	2.1975	2.0911	2.1974
10^5	1	59.2178	59.9361	59.8292	3.9496	3.9289	3.9502
10^5	10	57.5382	57.4327	57.3724	3.8817	3.8548	3.8837
10^5	100	47.4895	48.8831	49.0001	3.6524	3.6407	3.6744
10^5	1000	48.1087	48.4175	48.7041	3.6420	3.6581	3.6914
10^6	1	190.2591	193.7325	186.0280	6.5106	6.3222	6.0547
10^6	10	188.7059	189.7797	188.4033	6.4951	6.7288	6.7674
10^6	100	202.9567	188.1784	197.0433	7.1618	6.6849	7.2269
10^6	1000	203.6610	203.0634	194.8239	7.1929	6.8176	7.4162

Table 2. Asymptotic results for the nine models with *free slip* boundary conditions. Each value is calculated as the average of either $V_{\rm rms}$ or Nu from elapsed time 0.25 to 0.35.

Ra	Pr	$V_{\rm rms}$ GAIA	$V_{\rm rms}$ TLBM	$V_{\rm rms}$ StreamV	$V_{\rm rms}$(inf Pr) Bench	Nu GAIA	Nu TLBM	Nu StreamV	Nu (inf Pr) Bench
10^4	1	43.8644	44.1416	43.8499		4.9867	5.0103	4.9875	
10^4	10	42.7317	43.0695	42.7758		4.8703	4.8860	4.8620	
10^4	100	42.8608	43.1158	42.8147		4.8900	4.8977	4.8774	
10^4	1000	42.8821	43.1362	42.8264	42.8650	4.8933	4.8985	4.8802	4.8844
10^5	1	213.5101	216.5428	213.2021		11.7162	11.7501	11.7056	
10^5	10	198.5696	202.8932	200.1335		10.9062	10.9585	10.9285	
10^5	100	193.2970	195.4603	192.9620		10.5298	10.4897	10.5075	
10^5	1000	193.4660	195.3945	192.9663	193.2145	10.5408	10.4772	10.5127	10.5341
10^6	1	987.9038	1019.7103	970.8799		26.0767	24.9414	25.8593	
10^6	10	797.8585	845.2052	829.9934		19.8642	19.7807	20.5083	
10^6	100	758.6200	753.9583	740.3633		19.9635	18.7409	19.9568	
10^6	1000	832.9202	828.2744	832.9149	833.9898	21.8342	20.3057	21.9043	21.9725

4.2 Time-dependent solutions

Figs 4 to 9 show the time-dependent values of the space-averaged root mean square of the velocity field $V_{\rm rms}$ and Nusselt number Nu for the 24 benchmark simulations with both *no-slip* and *free slip* boundary conditions, for each Rayleigh number Ra = 10^4, 10^5 or 10^6 and Prandtl number Pr = 1, 10, 100, 1000. The top panels show the results of GAIA, the middle panels of TLBM and the bottom panels the ones of StreamV. $V_{\rm rms}$ results for the three codes show a pattern that is in agreement for both the low and intermediate Ra (10^4 and 10^5), regardless of the value of Pr and regardless of the fact that the solution displays very different regimes, ranging from a rapid convergence to steady-state (Ra = 10^4) to oscillatory behaviour (Ra = 10^5). Differences appear when transitioning to a chaotic dynamics (Ra = 10^6) where small fluctuations naturally produce long-term differences.

In summary the main results on which the three approaches converge are:

(i) Regardless of the boundary conditions, the flow for Ra = 10^4 is laminar, and evolves towards a steady-state solution whose $V_{\rm rms}$ and Nu values depend very weakly on Pr. Interestingly, $V_{\rm rms}$ displays more oscillations for *free slip* boundary conditions compared to *no-slip* and larger oscillations for Pr = 10 compared to either higher or lower Pr values, indicating the emergence of a resonance for this specific set of boundary conditions. For this low Ra value, the results at Pr = 100 and Pr = 1000 are nearly identical showing early convergence to infinite Pr solutions. We observe that TLBM

does not capture Nu solutions at Pr = 1000 showing a departure from Pr = 100 and Pr = 10, which are instead consistent with the other codes. Reasons for this are discussed in Section 5.

(ii) The results for Ra = 10^5 differ from the ones obtained at Ra = 10^4 being strongly dependent on the boundary conditions.

(a) For *no-slip* boundary conditions an oscillatory solution appears for Pr = 1 and dissipates within the time frame considered. It is almost completely absent for Pr = 10 but then reappears for Pr $\geq$ 100 where it shows wide $V_{\rm rms}$ and Nu oscillations and does not dissipate through time. We show snapshots of this oscillatory pattern in Fig. 10 where it is clear that *no-slip* boundary conditions favor the oscillations by the hot source at the sides and bottom of the domain. Even if this outcome is strongly dependent on the *no-slip* BCs, it is remarkable that it does not appear for any other Ra and Pr values. Pr = 1000 and Pr = 100 solutions of the three codes are almost indistinguishable, indicating early convergence to infinite Pr solutions.

(b) For *free slip* BCs, Ra = 10^5 solutions are remarkably different from *no-slip* BCs, but show features that already emerged in the Ra = 10^4 results. Damped oscillations appear for Pr = 1 but are considerably larger for Pr = 10 where they persist almost until the end of the simulation (elapsed time t = 0.35), whereas oscillations for larger Pr (100 and 1000) are damped very rapidly. Interestingly, the three methods all find a different transient solutions between Pr = 100 and Pr = 1000, suggesting that convergence to infinite
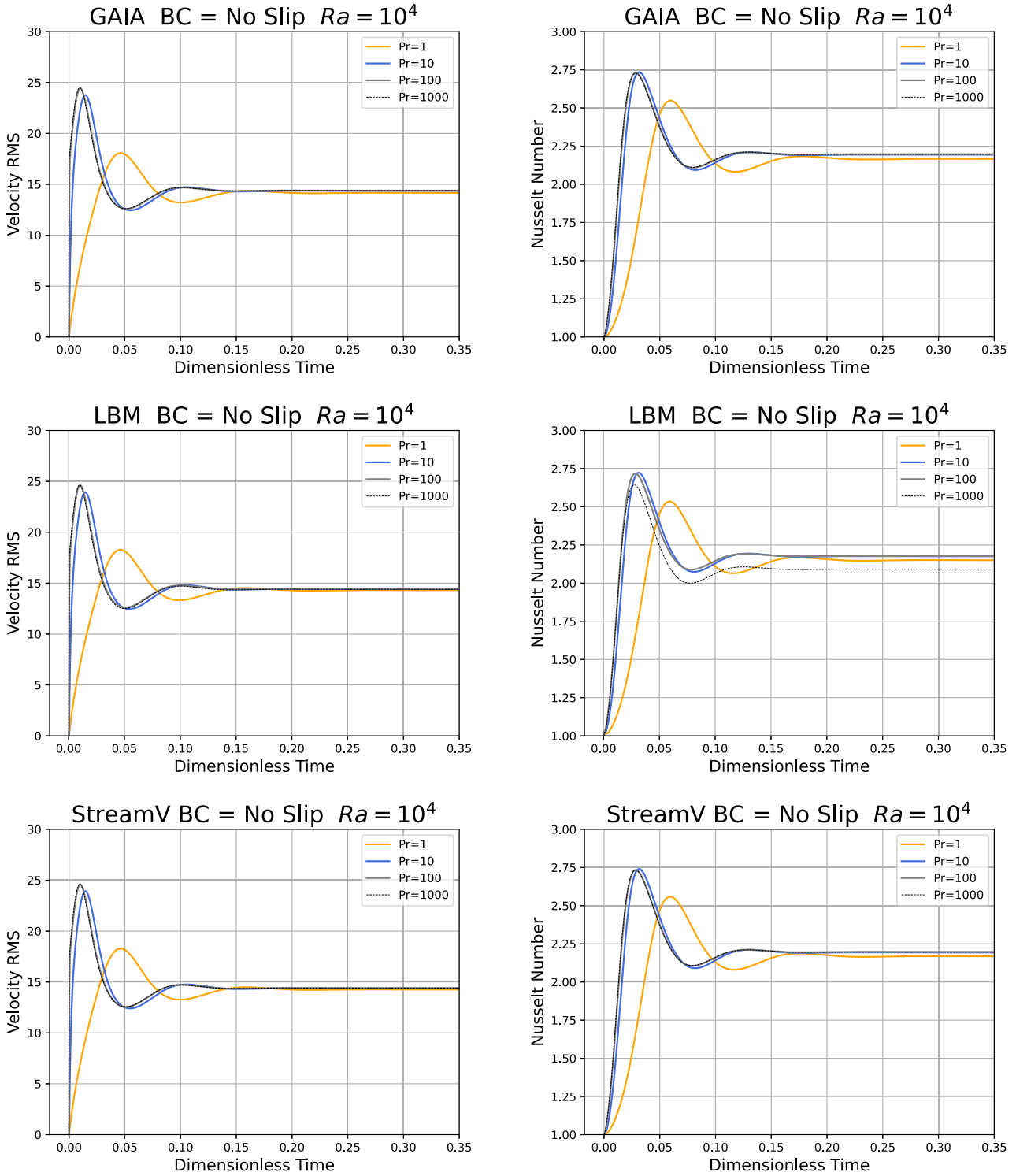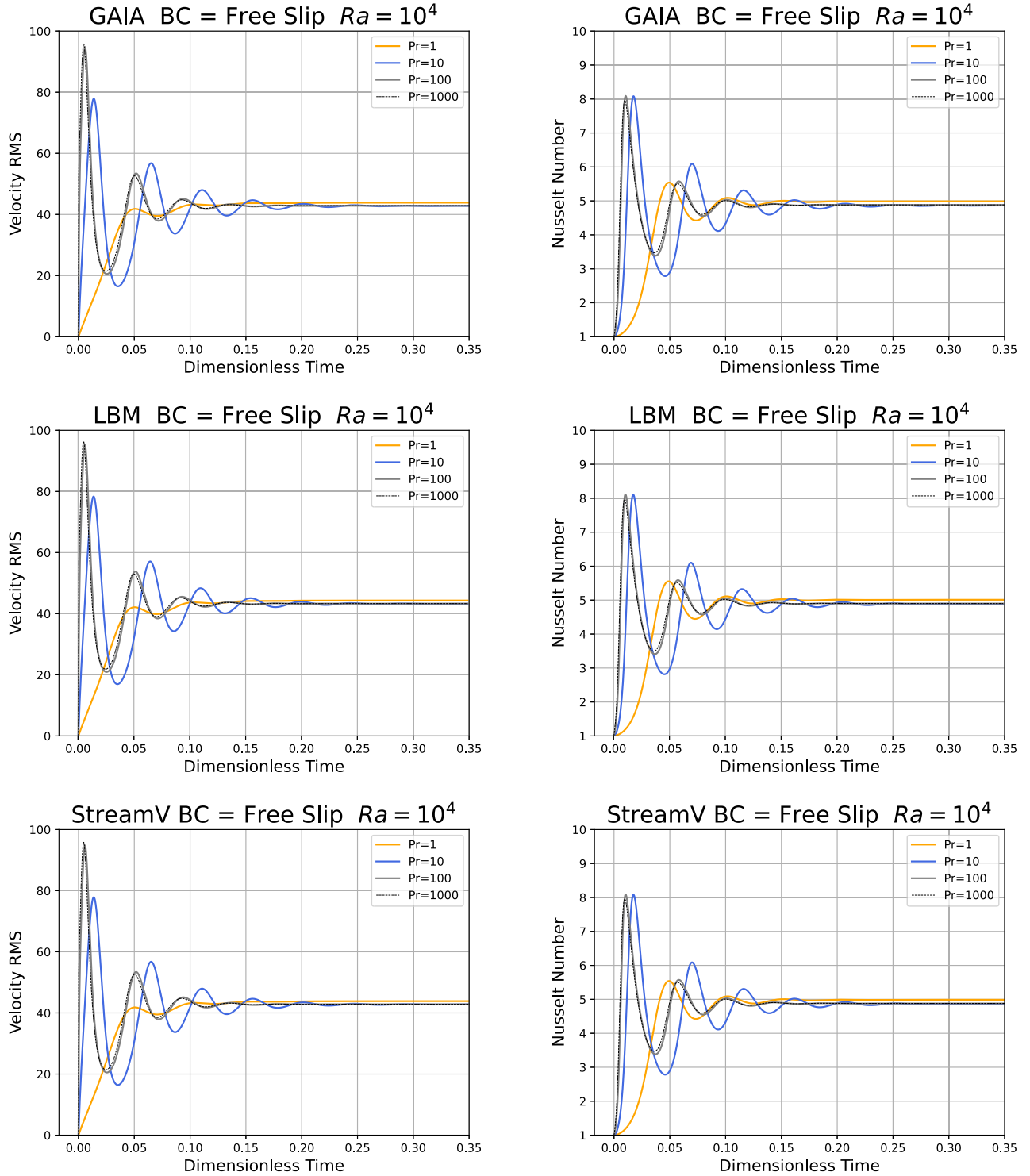
Figure 4. Comparison of the time evolution of V_{rms} (left) and Nusselt number Nu (right) for the `GAIA` (top), `TLBM` (middle) and `StreamV` (bottom) codes for Ra $= 10^4$ bounded by *no-slip* boundary conditions, for Prandtl numbers 1, 10, 100 and 1000. In the legend Pr $= 1000$ is placed last since this its graphs overlaps all others.

Pr requires at least Pr $= 1000$, even if the asymptotic is almost identical between Pr $= 100$ and Pr $= 1000$.

(iii) Solutions at Ra $= 10^6$ are again different between *free slip* and *no-slip* boundary conditions. Nevertheless, all codes show that for both BCs results are mildly oscillatory for Pr $= 1$ and quickly

converge to a steady-state solution, while for Pr ≥ 10 the dynamics becomes chaotic. This transition to chaos is unlikely related to *Reynolds* type of turbulence, due to the larger damping of the flow at high Pr, where momentum diffusion (kinematic viscosity) is higher compared to heat diffusion. This is further discussed in Section 5.
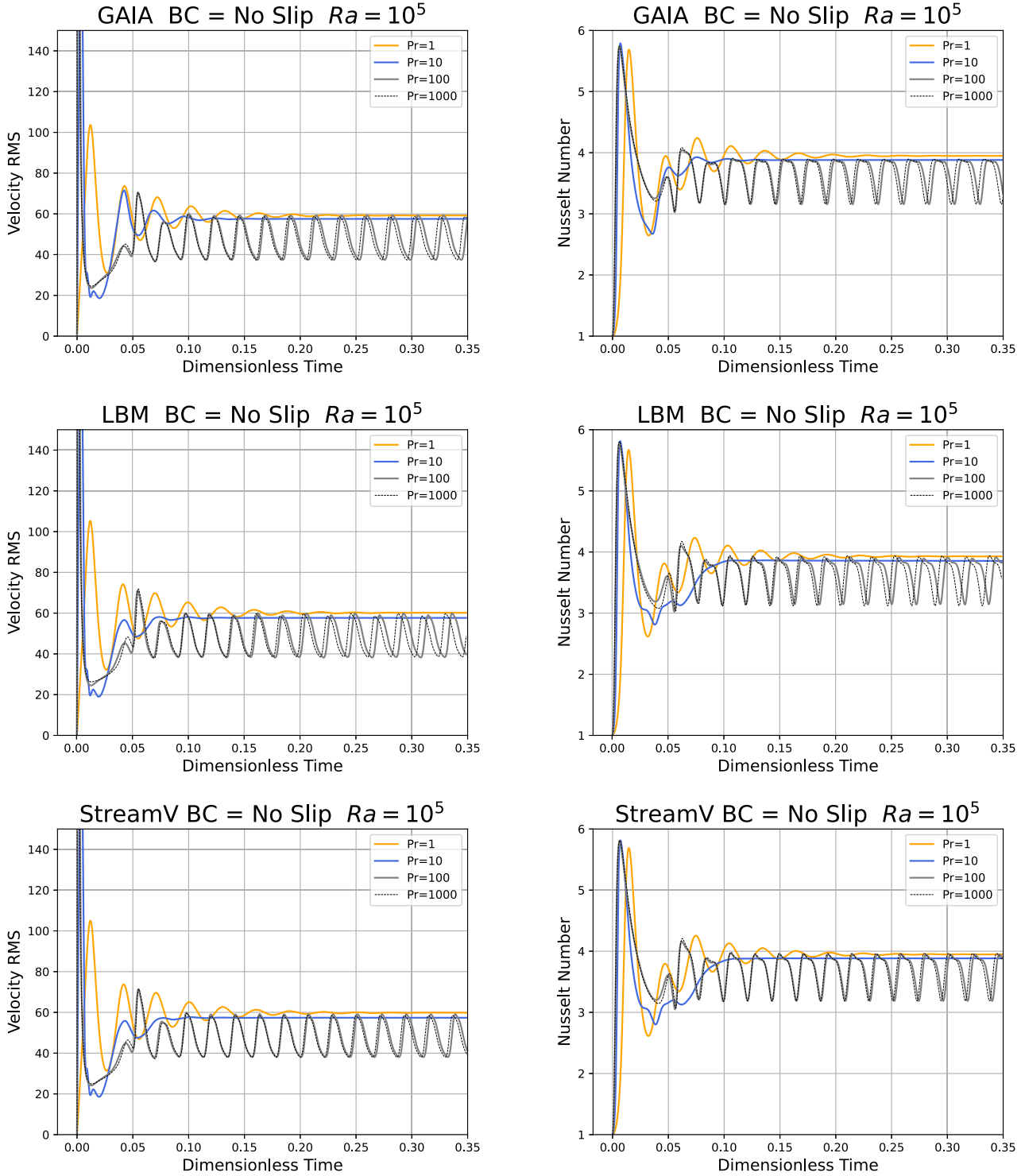
Figure 5. Time evolution of V_{rms} (right) and Nusselt number Nu (left) for the GAIA (top), TLBM (middle) and StreamV (bottom) codes for Ra $= 10^4$ with *free slip* boundary conditions, for Prandtl numbers 1, 10, 100 and 1000.

(a) For *no-slip* boundary conditions, Fig. 8 shows that for Pr ≥ 10, all methods agree that a chaotic behaviour appears with a frequency independent or very weakly dependent on Pr. Although the system does not converge to a unique steady-state solution, it stabilizes towards steady average V_{rms} and Nu, whose values are discussed in Section 4.1. Solutions for Pr ≥ 10 differ between the different modelling approaches, as expected for a chaotic system,

where the long-term solutions are highly dependent on small differences. Solutions for Pr $= 1000$ do not display substantial differences from smaller Pr, demonstrating early convergence to infinite Pr solutions, similarly to the other *no-slip* BCs solutions.

(b) *Free slip* BCs solutions, shown in Fig. 9, display the highest V_{rms} magnitude observed. Since, as shown below, the *Reynolds* number is Re $= V_{\mathrm{rms}}/$Pr, chaotic solutions are observed for low Re
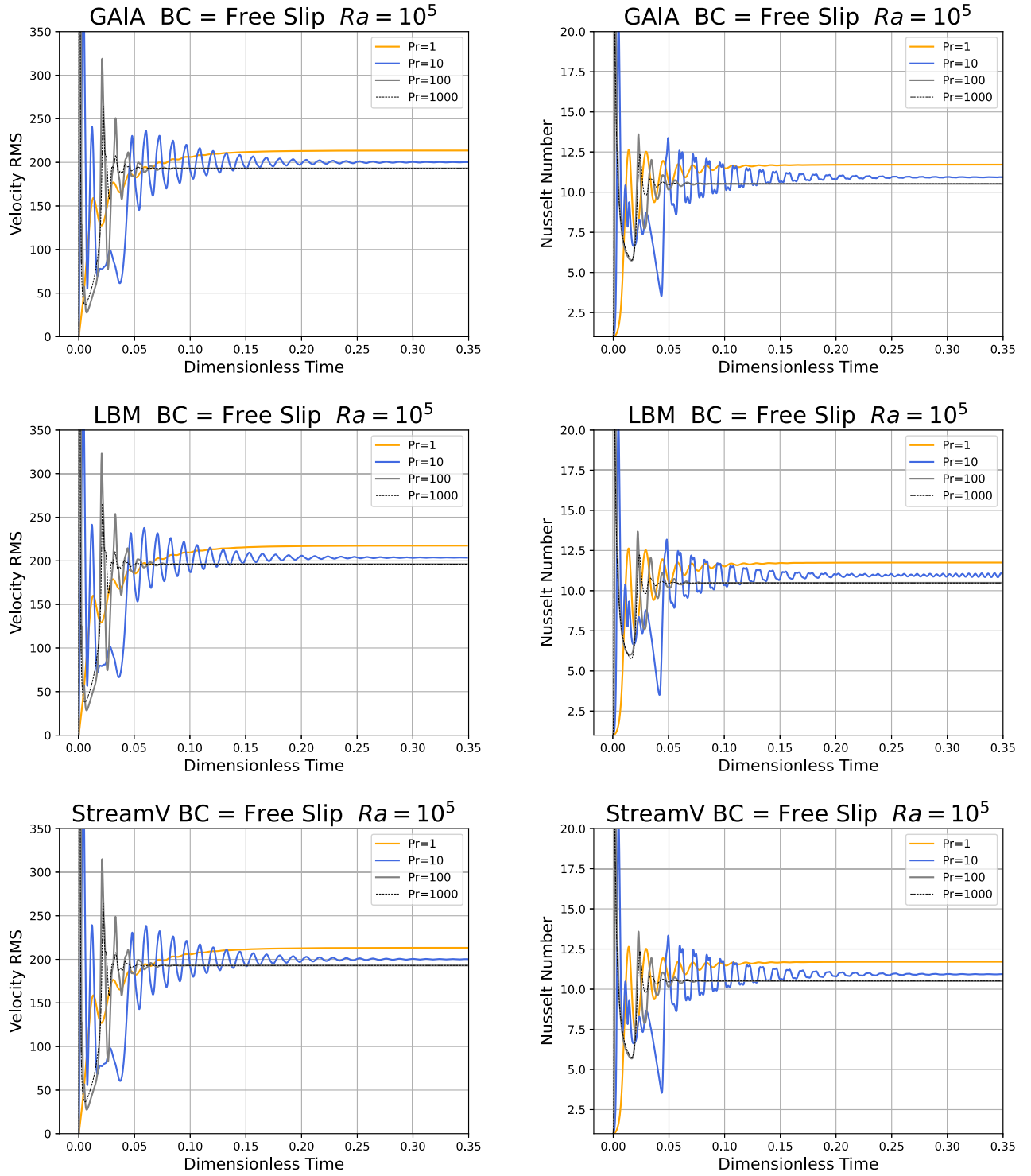
Figure 6. Comparison of the time evolution of $V_{\rm rms}$ (right) and Nusselt number Nu (left) for the `GAIA` (top), `TLBM` (middle) and `StreamV` (bottom) codes for Ra $= 10^5$ with *no-slip* boundary conditions, for Prandtl numbers 1, 10, 100 and 1000.

(high Pr), therefore they are unlikely caused by *Reynolds* type of turbulence. All methods show a transition to chaotic solutions for Pr ≥ 10, however with remarkably different outcomes, as discussed below. All three codes find that oscillations for Pr $= 10$ are small but become larger for Pr $= 100$, until all methods converge to similar steady-state solution for Pr $= 1000$, which matches the infinite Pr case, as discussed in Section 4.1.

4.3 Resolution test

The nominal spatial resolution adopted for each numerical code is very different, ranging from 64×64 for `StreamV` (except for cases at Ra $= 10^6$ and Pr $= 1$ where the nominal resolution was set to 128×128) to 150×150 for `GAIA` and 512×512 for `TLBM`, and was empirically chosen by each modeller depending on the knowledge of the employed software and on the computational power
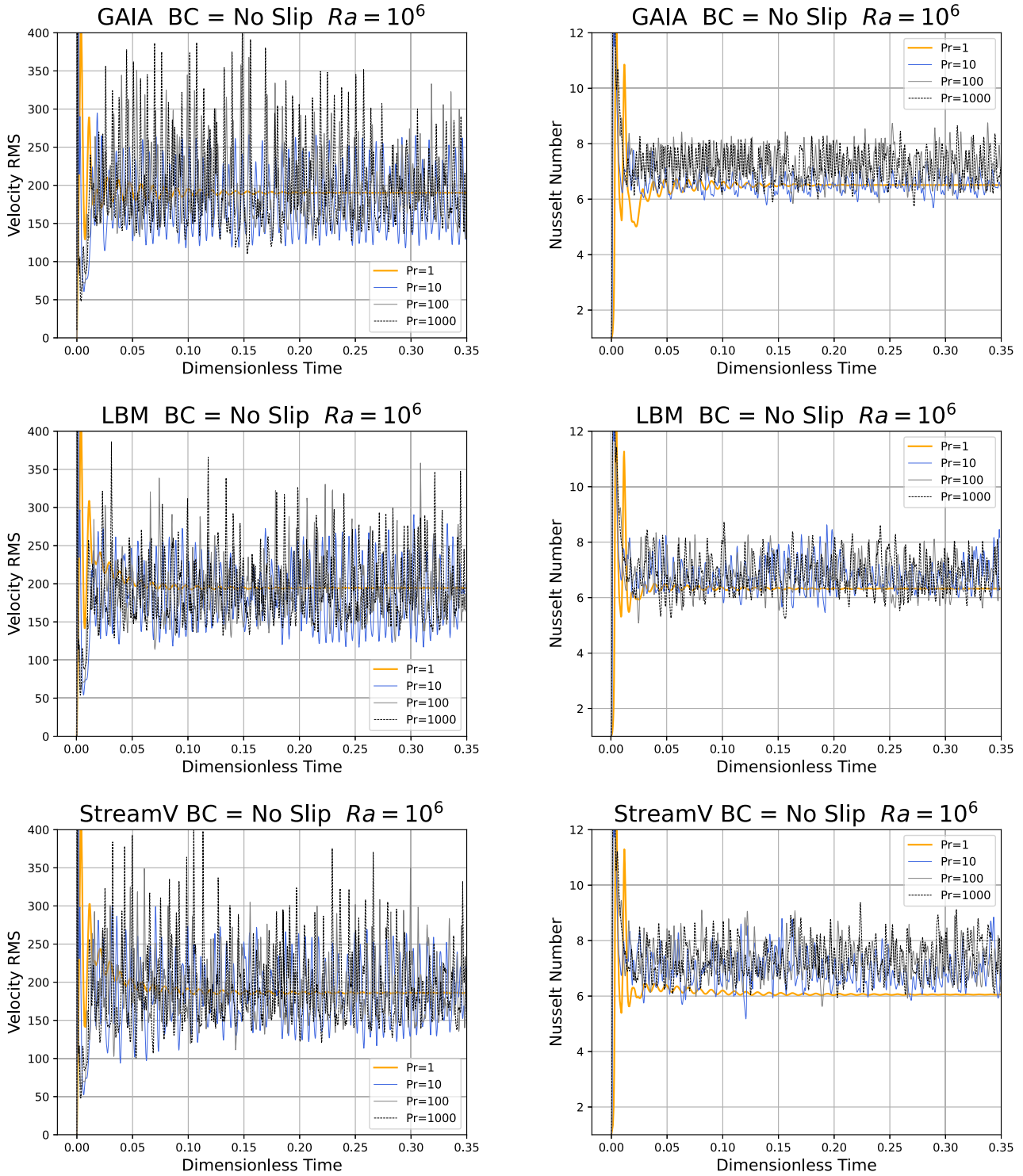
Figure 7. Comparison of the time evolution of $V_{\rm rms}$ (right) and Nusselt number Nu (left) for the `GAIA` (top), `TLBM` (middle) and `StreamV` (bottom) codes for Ra = 10^5 with by *free slip* boundary conditions, for Prandtl numbers 1, 10, 100 and 1000.

availability of each institution. To verify that the resolution was sufficient, we performed a resolution test for the 'most demanding' case corresponding to the highest Ra and lowest Pr values considered in our benchmarks, where the turbulence reaches its maximum requiring the finest resolution. For this case, we tested the *no-slip* boundary condition for the four resolutions: 64×64, 128×128,

256×256 and 512×512. The results for both $V_{\rm rms}$ and Nu are shown in Fig. 11.

We observe that all codes converge to the same solution for sufficiently high resolution. However, for this specific turbulent case, low resolution can result in different, likely incorrect, solutions. `StreamV` offers a good approximation of the common solution

Figure 8. Comparison of the time evolution of V_{rms} (right) and Nusselt number Nu (left) for the `GAIA` (top), `TLBM` (middle) and `StreamV` (bottom) codes for Ra = 10^6 with *no-slip* boundary conditions, for Prandtl numbers 1, 10, 100 and 1000.

already at a resolution of 64×64, and its solution already converges at a resolution of 128×128.

Because all other cases shown in this benchmark are less turbulent, the adopted 64×64 resolution is justified in this work with this code. Indeed, we checked that results obtained with `StreamV` for finer grids were not significantly different from those obtained

on a 64×64 grid for the other less turbulent cases. `TLBM` converges to the correct solution at a resolution of 256×256 for V_{rms} but requires 512×512 to obtain the correct Nu. Since all models in this benchmark were obtained with this code at this higher resolution, the results appear justified. `GAIA` reaches a good approximation of the common solution already at a resolution of
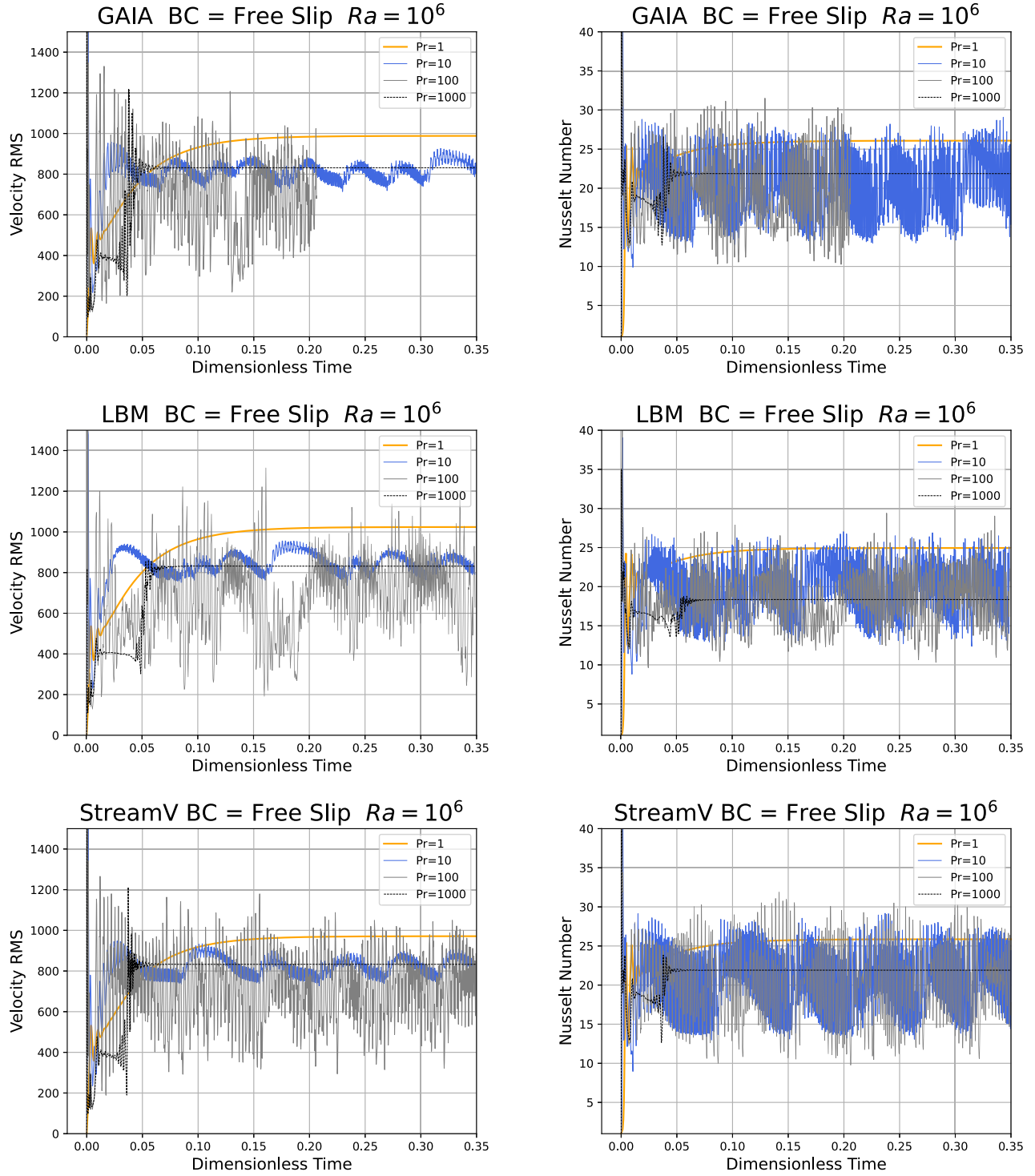
Figure 9. Comparison of the time evolution of V_{rms} (right) and Nusselt number Nu (left) for the `GAIA` (top), `TLBM` (middle) and `StreamV` (bottom) codes for Ra = 10^6 with by *free slip* boundary conditions, for Prandtl numbers 1, 10, 100 and 1000.

128×128, however the solution converges only for a mesh of 512×512 for this turbulent case. This provides an explanation for some discrepancies observed between the three codes with the nominal spatial resolution of 150×150 adopted for `GAIA` for all cases (except the resolution test). However, since the turbulence of this resolution test is the highest, we believe that the resolution was sufficient for most cases.

We tested the effect of the formalism used (primitive variables *versus* stream function) on the convergence and the accuracy of the solution by performing an additional set of resolution test with `StreamV` using a primitive variable formulation (see Section 3.2 for further details) on regular staggered grids with up to 256×256 square cells. The results are displayed in Fig. 11. We found that the primitive variable formulation solutions compare well with the
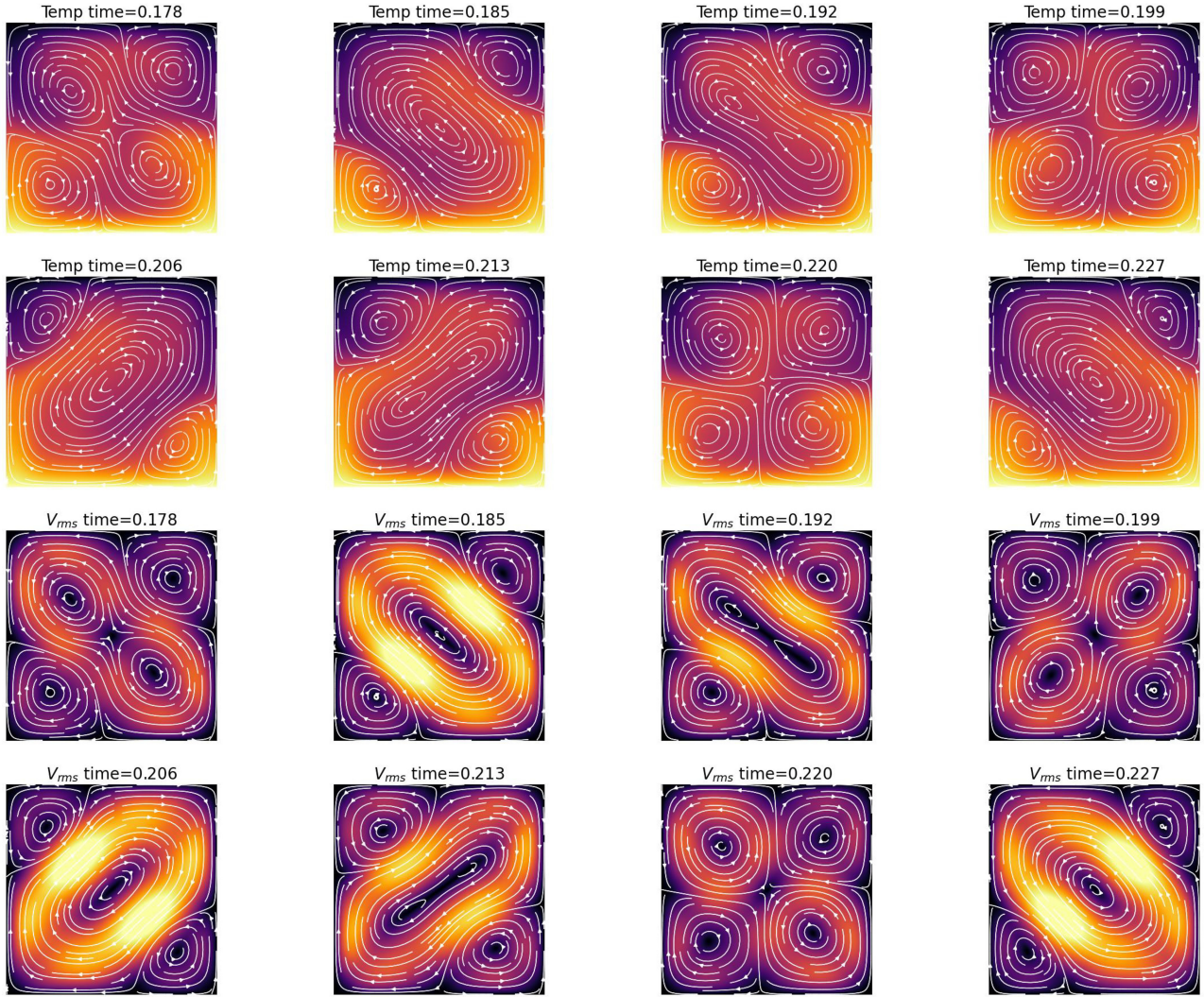
Figure 10. Sequence of snapshots of the oscillatory mode with *no-slip* boundary conditions for Pr = 100 and Ra = 10^5. Top: temperature ($T_{min} = 0$ and $T_{max} = 1$). Bottom: root mean square of the velocity ($V_{min} = 0$ and $V_{max} = 100$).

stream function solutions both in terms of accuracy and convergence rate. This indicates that the formulation does not play a significant role, in agreement with previous works (Deubelbeiss & Kaus 2008). This suggests that the faster convergence rate for `StreamV` may be due to differences in solving the conservation of energy between the three different codes.

5 DISCUSSION

While all codes predicted the same general dynamics, the origin of some discrepancies are worth being discussed. Interestingly, there are no two codes that agree on every solutions. Yet, often two codes show matching solutions with the third slightly differing. This does not demonstrate that the two matching codes show the correct solutions; however, it offers indications.

Differences between solutions of the three codes for Ra = 10^4 are virtually absent for both *no-slip* and *free slip* boundary conditions (Fig. 4) (Fig. 5 and Section 4.1). For Ra = 10^5, Pr = 10 and *no-slip* BC, only TLBM and `StreamV` show matching solutions in the transient phase ($t < 0.1$) (Fig. 6). For the oscillatory solution (Pr = 100 and Pr = 1000), only a mild time-shift appears between the two

Pr cases, different for the three codes, less for `StreamV` and more for `TLBM`, but not larger than $\Delta t \leq 0.01$.

5.1 Regime diagram for oscillatory and chaotic solutions

Our results show a richer set of solutions than initially anticipated. Indeed, we expected a more predictable transition from low to high Pr and from low Ra to high Ra. To better understand how the system transitions from a steady to oscillatory mode for *no-slip* boundary conditions and $R = 10^5$, we tested a wide range of intermediate values, besides the ones of the benchmark and found a sudden transition at Pr ≈ 10. The V_{rms} for values of Pr between 7 and 14 are shown in Fig. 12. For lower values, the system is steady, while for a greater Pr oscillations suddenly appear all with comparable amplitudes. Observation of the oscillatory solution shows that it is related to the fixed boundary conditions in temperature, which are a consequence of the zero velocity at the boundary of the domain. The spontaneous emergence of the oscillations can be also seen as the result of a competition between momentum and thermal diffusion, since Pr is the ratio of these two processes.
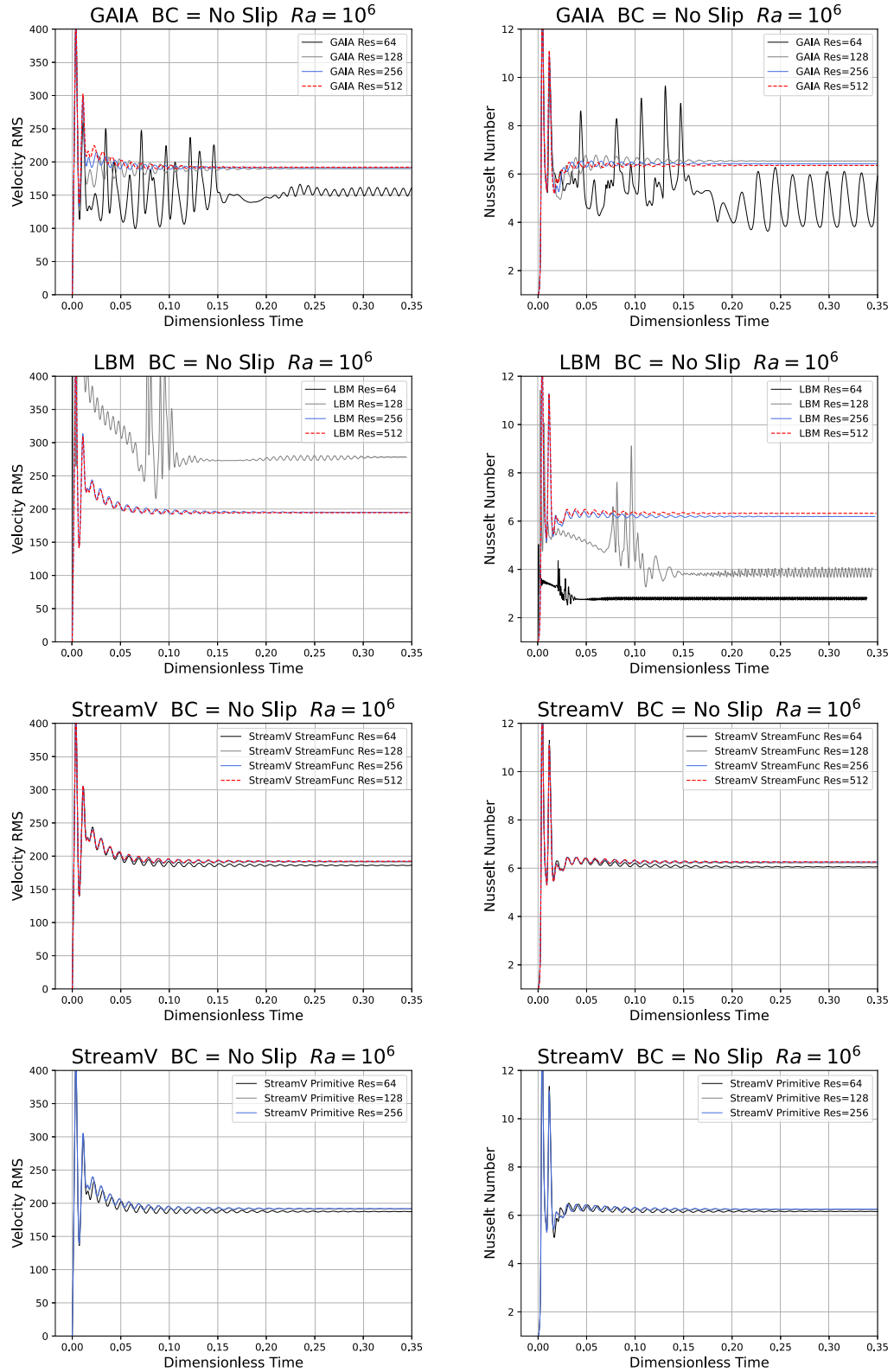
Figure 11. Resolution test of the `GAIA` (top), `TLBM` (middle) and two versions of the `StreamV` (bottom) codes for the Ra = 10^6 bounded by *no-slip* boundary conditions, and Pr = 1. All codes converge to the same solution. `StreamV` converges at a coarser resolution regardless whether *stream function* or the *primitive variables* formulation is chosen.
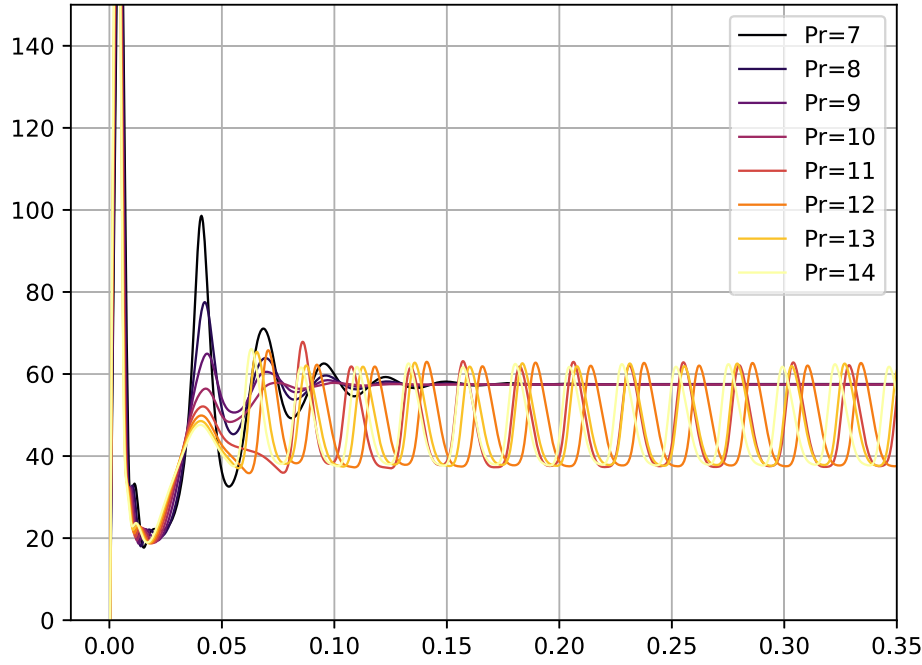
Figure 12. TLBM solutions of V_{rms} for the Ra $= 10^5$ and *no slip* boundary conditions for Prandtl number values in the vicinity of Pr ≈ 10. These results were confirmed by a set of solutions obtained with `StreamV`.

It would be certainly interesting to fully map the dependency of the transition to the oscillatory behaviour in function of Ra and Pr, given that one can speculate that the critical Pr at which the transition emerges is related to Ra. As shown in previous works that have investigated Pr dependent transitions to oscillatory and chaotic system of fluid-dynamic cases, this will likely also depend on the box geometry and initial conditions Henry & Buffat (1998) and Stojanović *et al.* (2024). This type of setup can have implications in volcanology, where *pulsating*, repetitive periodic dynamics are common, Pr is in the same ballpark *no-slip* boundary conditions can mimic a volcanic conduit. We believe that a more accurate model for the implication of this solution to geophysical problems such as volcanic conduits should be done in a separate dedicated study.

Interesting behaviour also emerge for *free-slip* boundary conditions. For example, damped oscillations appear at intermediate Pr values for Ra $= 10^5$ while for both smaller and larger Pr values, they do not appear. This kind of *resonance* is likely related to the same physics behind the oscillations in the *no slip* case. For higher energies (Ra $= 10^6$) the oscillations become chaotic fluctuations. Similar to the Ra $= 10^5$ case, we explored the Pr-controlled dynamic transition from steady state (Pr $= 1$) to chaos (Pr $= 10$, 100) and then back to steady state (Pr $= 1000$). We tested Pr $= 4, 8, 16, 32, 64, 128, 256, 512, 1024$ and measured the standard deviation of V_{rms} in the final stage of the simulations (elapsed time $t > 0.25$), representative of the asymptotic results (Fig. 13). In contrast to the transition to an oscillatory pattern, the transition to chaos and back is smooth, starting between Pr ≈ 8 and Pr ≈ 10, it then reaches a peak just before Pr ≈ 100 and then decreases until a more laminar flow appears again for Pr ≈ 200. In this case as well, a map of the transitions should be developed in function of both Pr and Ra. Possibly, lateral boundary conditions could be involved, as well as the domain aspect ratio, and conditions might change in 3-D. This interesting investigation extends beyond the purpose of this work.

Although we observe chaotic solutions at Ra $= 10^6$, they are likely not related to Kolmogorov turbulence, which becomes

significant at high *Reynolds* numbers (Re). This is evident for the most energetic case, characterized by the higher speeds, Ra $= 10^6$, where chaos is present at intermediate values of Pr. One can demonstrate that this chaotic solution is not related to Re. Re can be directly extrapolated from V_{rms}. The renormalized value of V_{rms} is $V\,L/\kappa$ where V is the solution emerging from each code, and κ is the thermal diffusivity. One obtains that the renormalized root mean square of the velocity is $V_{\mathrm{rms}} = V\,(L/\nu)\,(\nu/\kappa) = \mathrm{Re\,Pr}$. Since V_{rms} remains of the same order of magnitude with increasing Pr, then Re is inversely proportional to Pr, which is at odd with the observation that chaos initiates at a sufficiently high value of Pr. This implies that Kolmogorov turbulence is not causing these chaotic solutions. In general, for Kolmogorov driven turbulence at Pr ≈ 1, Re $\approx \mathrm{Ra}^{0.4-0.5}$ (e.g. Grossmann & Lohse 2000; Salvador & Samuel 2023; Walbecq *et al.* 2024, and references therein), for Pr $= 1$, but Kolmogorov turbulence becomes dominant only at much higher Ra.

The richness of these results suggest that intermediate Prandtl number simulations Pr $\in [1 - 1000]$ should be carefully investigated for the potential applications in geodynamics and volcanology, but this goes beyond the scope of this paper.

5.2 Thermal Lattice Boltzmann Method at high Prandtl Number

For the highest Pr value tested (Pr $= 1000$), TLBM asymptotically differs of a few percent from the other two codes and from established infinite Pr solutions, when they are available. Examples are Ra $= 10^6$ and *free slip* where both `StreamV` and `GAIA` are within 0.1 per cent from the known solution, while `TLBM` is about 1 per cent off from the known value. Correspondingly, Nu is about 7 per cent below the expected value. A similar discrepancy is present for the asymptotic Nu value of Ra $= 10^4$, Pr $= 1000$, *no-slip*, where Nu is 5 per cent lower from matching `StreamV` and `GAIA` solutions.

Our tests have shown that increasing numerical precision of the TLBM simulations from 32 to 64 bits has improved the solutions
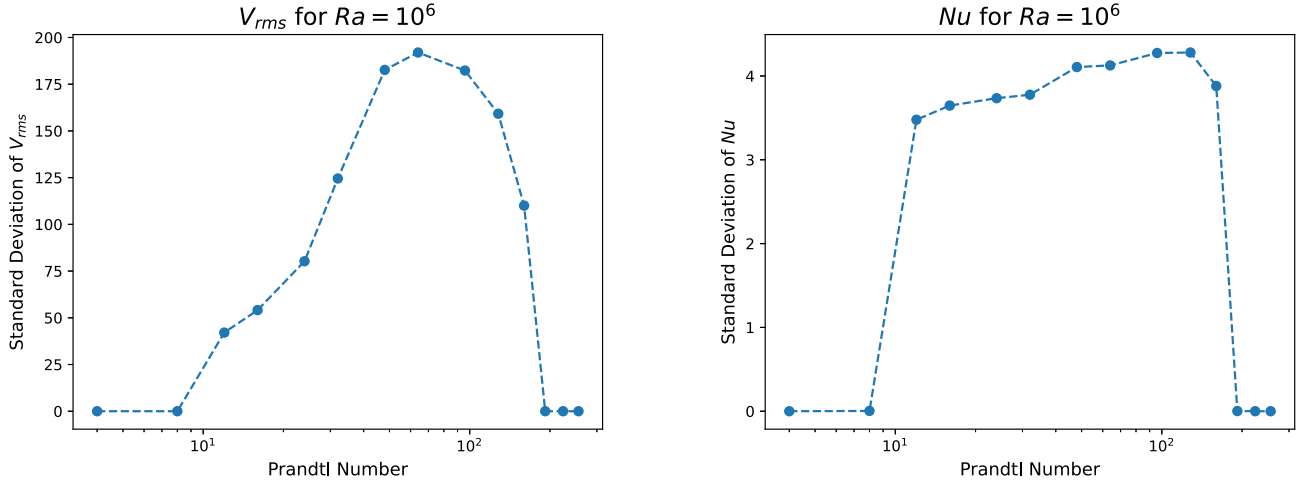
Figure 13. Standard deviation of V_{rms} and of Nu in function of Pr for the Ra $= 10^6$ and *free slip* boundary conditions for increasing powers of two of Pr obtained with the `TLBM` code for time > 0.1. The non-zero values of the standard deviation is an indicator of the intensity of the fluctuations.

at very high Pr. This can be understood by looking at the Mach numbers of each case. Focusing only on the *free slip* cases, where speeds are greater, for Ra $= 10^4$ the maximum measured Mach number at any step in the second half of the simulations is between $0.000\,44$ and 0.0022, for Ra $= 10^5$ it is between 0.0023 and 0.011, however for Ra $= 10^6$ it is between 0.028 and 0.092 (Pr $= 100$). Because compressibility affects fluid-dynamic solutions more at greater Mach numbers, Mach numbers between 0.05 and 0.09 could possibly justify some discrepancies. However in consideration that these are the highest values reached in the entire domain, across 500 recorded timesteps, we suggest an alternative explanation.

As detailed in Section 3.3, for very high Pr such as Pr $= 1000$, kinematic viscosity is 1000 times greater than thermal diffusivity. Since the momentum relaxation time $\tau_f = 0.5 + \nu/c^2 = 0.5 + 3 * \nu$ and similarly $\tau_g = 0.5 + 3 * \kappa$, when Pr is very high, κ must be extremely low, and therefore high numerical precision is necessary to correctly calculate the relaxation of the thermal energy density g.

Our implementation of the couple of thermal and momentum solvers in LBM is only one of the possible approaches to the problem. An alternative method was proposed in Parmigiani *et al.* (2009) where they introduced a new multiscale approach based on the implicit dependence of the Pr number on the relaxation time.

5.3 Computational efficiency

So far, we did not discuss the computational efficiency of the different approaches. Since they are based on distinct assumptions and approximations converging towards the solution of the NS equations, the methods are expected to perform differently at distinct Pr.

`TLBM` works optimally for Pr ≈ 1 since the relaxation times τ_f and τ_g are equal. A new version of the code, not used in this benchmark, has been just developed, in which the timestep is adaptive, based on a different lattice viscosities calibrated to maintain the relaxation time not too close to 0.5 while at the same time keep the Mach number sufficiently low. Its testing is however postponed to a follow up publication. Regarding parallel performance, because it requires no matrix operations, `TLBM` scales linearly on HPC (High-Performance

Computing) clusters, as demonstrated elsewhere up to 300 000 cores (Mora *et al.* 2024).

`GAIA` is also more efficient at smaller Pr, based on its present formulation which is based on treating the $1/$Pr term of the NS equations as a forcing term and iterating. With increasing Pr, the spectral radius of the Navier Stokes equations increases, therefore requiring many more iterations. For example for the *free-slip* and Ra $= 10^6$ case, The number of iterations necessary to reach a 10^{-8} tolerance are 1930 for the infinite Pr case, 94 for Pr $= 100$ and just 68 for Pr $= 1$.

The specific formulation used in `StreamV` is optimal for low Pr numbers because of the explicit time stepping used (see eq. 11). For large Pr values (> 10) the time step becomes smaller than the one associated with an advective CFL (Courant-Friedrichs-Lewy) criterion. This limitation could, however, be removed by using high-order semi-implicit schemes.

6 CONCLUSIONS

To benchmark existing codes that model convection at low Prandtl numbers, we proposed and performed tests, all confined in a 1×1 box, with the same thermal boundary conditions ($T = 1$ at the bottom, $T = 0$ at the top) and varying Rayleigh number as in previous benchmarks (Ra $= 10^4$, Ra $= 10^5$, Ra $= 10^6$) (Blankenbach *et al.* 1989a). We extended previous benchmarks by considering the effect of a finite Prandtl number, by considering four values of Pr, which cover the cases ranging from the magma ocean stage (Pr $= 1$) to quasi solid-state mantle convection (Pr $= 1000$), comparing the outcome of intermediate values (Pr $= 10$ and Pr $= 100$) as well. For every set of values, we tested two types of boundary conditions (*no-slip* and *free slip*). All the combinations form a total suite of 24 cases.

While several previous benchmarks (e.g. Blankenbach *et al.* 1989a) focused on testing the steady-state solution, we find that by investigating the transient from a common initial condition it is possible to explore sometimes unexpected behaviours, such as the ones found at intermediate Prandtl numbers (Pr $= 10$ to Pr $= 100$), as well as unexpected effects observed when changing the velocity boundary conditions. Overall, notwithstanding occasional differences, the three codes broadly showed the same outcome and transition from steady to oscillatory and to turbulent behaviour for the same Pr, Ra and BCs. We therefore conclude that the distinct

approaches used for the different codes are suitable and reliable for geodynamic investigation of systems ranging from a magma ocean to solid-state mantle convection, across volcanic to planetary scales.

CONFLICT OF INTEREST

There are no conflicts of interest.

DATA AVAILABILITY

The time-series of V_{rms} and Nu number for the 24 benchmark cases and for each code are uploaded on a repository available on Zenodo: https://doi.org/10.5281/zenodo.13625159

REFERENCES

Ali Boroumand, M., Morra, G. & Mora, P., 2024. Extracting fundamental parameters of 2-D natural thermal convection using convolutional neural networks, *J. Appl. Phys.,* **135**(14). doi:10.1063/5.0198004.

Amestoy, P.R., Duff, I.S., Koster, J. & L'Excellent, J.-Y., 2001. A fully asynchronous multifrontal solver using distributed dynamic scheduling, *SIAM Journal on Matrix Analysis and Applications,* **23**(1), 15–41.

Amestoy, P.R., Guermouche, A., L'Excellent, J.-Y. & Pralet, S., 2006. Hybrid scheduling for the parallel solution of linear systems, *Parallel Computing,* **32**(2), 136–156.

Ballmer, M.D., Lourenço, D.L., Hirose, K., Caracas, R. & Nomura, R., 2017. Reconciling magma-ocean crystallization models with the present-day structure of the earth's mantle, *Geochem. Geophys. Geosyst.,* **18**(7), 2785–2806.

Bhatnagar, P.L., Gross, E.P. & Krook, M., 1954. A model for collision processes in gases. i. small amplitude processes in charged and neutral one-component systems, *Phys. Rev.,* **94**(3), 511. doi:10.1103/PhysRev.94.511.

Blankenbach, B. *et al.*, 1989a. A benchmark comparison for mantle convection codes, *Geophys. J. Int.,* **98**(1), 23–38.

Blankenbach, B. *et al.*, 1989b. A benchmark comparison for mantle convection codes, *Geophys. J. Int.,* **98**(1), 23–38.

Brandt, A., 1977. Multi-level adaptive solutions to boundary-value problems, *Math. Comput.,* **31**(138), 333. doi:10.1090/S0025-5718-1977-0431719-X.

Chen, S. & Doolen, G.D., 1998. Lattice boltzmann method for fluid flows, *Ann. Rev. Fluid Mech.,* **30**(1), 329–364.

Chorin, A., 1968. Numerical solution of the Navier–Stokes equations, *J. Comput. Phys.,* **22**, 745–762.

Christensen, U.R. *et al.*, 2001. A numerical dynamo benchmark, *Phys. Earth planet. Inter.,* **128**(1–4), 25–34.

Dellar, P.J., 2002. Lattice kinetic schemes for magnetohydrodynamics, *J. Comput. Phys.,* **179**(1), 95–126.

Deubelbeiss, Y. & Kaus, B.J., 2008. Comparison of Eulerian and Lagrangian numerical techniques for the Stokes equations in the presence of strongly varying viscosity, *Phys. Earth. planet. Inter.,* **171**, 92–111.

Erturk, E., Corke, T.C. & Gökçöl, C., 2005. Numerical solutions of 2-D steady incompressible driven cavity flow at high reynolds numbers, *Int. J. Numer. Methods Fluids,* **48**(7), 747–774.

Fleury, A., Plesa, A.-C., Hüttig, C. & Breuer, D., 2024. Assessing the accuracy of 2-D planetary evolution models against the 3-d sphere, *Geochem. Geophys. Geosyst.,* **25**(2), e2023GC011114. doi:10.1029/2023GC011114.

Ghia, U., Ghia, K.N. & Shin, C.T., 1982. High-Re solutions for incompressible flow using the navier-stokes equations and a multigrid method, *J. Sci. Comput.,* **48**, 387–411.

Grossmann, S. & Lohse, D., 2000. Scaling in thermal convection: A unifying theory, *J. Fluid Mech.,* **407**, 27–56.

Gunawardana, P.M., Chowdhury, P., Morra, G. & Cawood, P.A., 2024. Correlating mantle cooling with tectonic transitions on early earth, *Geology.***52**(4), 230–234.

Harten, A., 1983. High resolution schemes for hyperbolic conservation laws, *J. Sci. Comput.,* **49**, 357–393.

Henry, D. & Buffat, M., 1998. Two-and three-dimensional numerical simulations of the transition to oscillatory convection in low-prandtl-number fluids, *J. Fluid Mech.,* **374**, 145–171.

Honarbakhsh, L., Morra, G., Mora, P. & Jackson, C., 2025. Metal-Silicate Segregation During Planetary Accretion via the Multiphase Thermal Lattice Boltzmann Method: Implications on Silicate Entrainment and Iron-Silicate Mixing, in *Journal of Geophysical Research - Solid Earth* in Review.

Houston, M.H. & De Bremaecker, J.C., 1974. ADI solution of free convection in a variable viscosity fluid, *J. Sci. Comput.,* **16**, 221–239.

Huang, H., Sukop, M. & Lu, X., 2015. *Multiphase Lattice Boltzmann Methods: Theory and Application,* John Wiley & Sons.

Hüttig, C. & Stemmer, K., 2008a. Finite volume discretization for dynamic viscosities on voronoi grids, *Phys. Earth planet. Inter.,* **171**(1–4), 137–146.

Hüttig, C. & Stemmer, K., 2008b. The spiral grid: A new approach to discretize the sphere and its application to mantle convection, *Geochem. Geophys. Geosyst.,* **9**(2). doi:10.1029/2007GC001581.

Hüttig, C., Tosi, N. & Moore, W.B., 2013. An improved formulation of the incompressible navier–stokes equations with variable viscosity, *Phys. Earth planet. Inter.,* **220**, 11–18.

Jiang, G.S. & Shu, C.W., 1996. Efficient implementation of Weighted ENO schemes, *J. Sci. Comput.,* **126**, 202–228.

King, S.D., Lee, C., Van Keken, P.E., Leng, W., Zhong, S., Tan, E., Tosi, N. & Kameyama, M.C., 2010. A community benchmark for 2-d cartesian compressible convection in the earth's mantle, *Geophys. J. Int.,* **180**(1), 73–87.

Kooij, G.L. *et al.*, 2018. Comparison of computational codes for direct numerical simulations of turbulent rayleigh–bénard convection, *Comput. Fluids,* **166**, 1–8.

Korenaga, J., 2010. On the likelihood of plate tectonics on super-earths: does size matter?, *Astrophys. J. Lett.,* **725**(1), L43. doi:10.1088/2041-8205/725/1/L43.

Korenaga, J. & Marchi, S., 2023. Vestiges of impact-driven three-phase mixing in the chemistry and structure of earth's mantle, *Proc. Natl. Acad. Sci. USA,* **120**(43), e2309181120. doi:10.1073/pnas.2309181120.

Krüger, T., Kusumaatmaja, H., Kuzmin, A., Shardt, O., Silva, G. & Viggen, E.M., 2017. *The Lattice Boltzmann Method,* Vol. **10,** pp. 4–15, Springer International Publishing.

Kupferman, R., 2001. A central-difference scheme for a pure stream function formulation of incompressible viscous flow, *SIAM J. Sci. Comput.,* **23,** 1–18.

Leonardi, A., Wittel, F.K., Mendoza, M. & Herrmann, H.J., 2015. Lattice-boltzmann method for geophysical plastic flows, *Recent Advances in Modelling Landslides and Debris Flows,* pp. 131–140. Springer Nature.

Lichtenberg, T., Bower, D.J., Hammond, M., Boukrouche, R., Sanan, P., Tsai, S.-M. & Pierrehumbert, R.T., 2021. Vertically resolved magma ocean–protoatmosphere evolution: H2, h2o, co2, ch4, co, o2, and n2 as primary absorbers, *J. Geophys. Res.: Planets,* **126**(2), e2020JE006711. doi:10.1029/2020JE006711.

Lohse, D. & Shishkina, O., 2023. Ultimate turbulent thermal convection, *Phys. Today,* **76**(11), 26–32.

Marchi, S., Bottke, W., Elkins-Tanton, L., Bierhaus, M., Wuennemann, K., Morbidelli, A. & Kring, D., 2014. Widespread mixing and burial of earth's hadean crust by asteroid impacts, *Nature,* **511**(7511), 578–582.

Mora, P. & Yuen, D.A., 2018. Simulation of regimes of convection and plume dynamics by the thermal lattice boltzmann method, *Phys. Earth planet. Inter.,* **275,** 69–79.

Mora, P., Morra, G., Yuen, D.A. & Juanes, R., 2021. Influence of wetting on viscous fingering via 2d lattice boltzmann simulations, *Transport in Porous Media,* **138**(3), 511–538.

Mora, P., Morra, G. & Yuen, D.A., 2023. Models of plate tectonics with the lattice boltzmann method, *Artificial Intelligence in Geosciences,* **4,** 47–58.

Mora, P., Morra, G., Honarbakhsh, L., Huttig, C. & Tosi, N., 2024. Progress and perspectives on using the lattice boltzmann method for geodynamics simulation research, *EGU General Assembly Conference Abstracts,* 14391.

Morra, G. & Tufo III, H.M., 2024. In memory of professor david alexander yuen, *Earthq. Res. Adv.,* **4**(2), 100 291. doi:10.1016/j.eqrea.2024.100291.

Nicolas, X., Medale, M., Glockner, S. & Gounand, S., 2011. Benchmark solution for a three-dimensional mixed-convection flow, part 1: Reference solutions, *Numerical Heat Transfer, Part B: Fundamentals,* **60**(5), 325–345.

Nikolaou, A., Katyal, N., Tosi, N., Godolt, M., Grenfell, J.L. & Rauer, H., 2019. What factors affect the duration and outgassing of the terrestrial magma ocean?, *Astrophys. J.,* **875**(1), 11. doi:10.3847/1538-4357/ab08ed.

Parmigiani, A., Huber, C., Chopard, B., Latt, J. & Bachmann, O., 2009. Application of the multi distribution function lattice boltzmann approach to thermal flows, *Eur. Phys. J. Special Topics,* **171,** 37–43.

Patankar, S.V., 1980. *Numerical Heat Transfer and Fluid Flow,* Hemisphere Publishing Corporation, New York.

Patočka, V., Calzavarini, E. & Tosi, N., 2020. Settling of inertial particles in turbulent rayleigh-bénard convection, *Phys. Rev. Fluids,* **5,** 114 304.

Peng, Y., Shu, C. & Chew, Y., 2003. Simplified thermal lattice boltzmann model for incompressible thermal flows, *Phys. Rev. E,* **68**(2), 026 701. doi:10.1103/PhysRevE.68.026701.

Ricard, Y., 2007. Physics of mantle convection, *Treatise on Geophysics,* **7,** 31–87.

Salvador, A. & Samuel, H., 2023. Convective outgassing efficiency in planetary magma oceans: insights from computational fluid dynamics, *Icarus,* **390**. doi:10.1016/j.icarus.2022.115265.

Salvador, A. et al., 2023. Magma ocean, water, and the early atmosphere of venus, *Space Sci. Rev.,* **219**(7), 51. doi:10.1007/s11214-023-00995-7.

Samuel, H., 2012. A re-evaluation of metal diapir breakup and equilibration in terrestrial magma oceans, *Earth. Planet. Sci. Lett.,* **313–314,** 105–114.

Samuel, H., 2014. A level set two-way wave equation approach for eulerian interface tracking, *J. Comput. Phys.,* **259,** 617–634.

Samuel, H., 2018. A deformable particle-in-cell method for advective transport in geodynamic modelling, *Geophys. J. Int.,* **214,** 1744–1773.

Samuel, H. & Evonuk, M., 2010. Modelling advection in geophysical flows with particle level sets, *g-cubed,* **11**(Q08020). doi:10.1029/2010GC003081.

Samuel, H., Ballmer, M.D., Padovan, S., Tosi, N., Rivoldini, A. & Plesa, A.-C., 2021. The thermo-chemical evolution of Mars with a strongly stratified mantle, *J. Geophys. Res.: Planets,* **126**(4), 1–61.

Solomatov, V., 2007. Magma oceans and primordial mantle differentiation, *Evolution of the Earth,* **9,** 91–119.

Stojanović, M., Romanò, F. & Kuhlmann, H.C., 2024. High-prandtl-number thermocapillary liquid bridges with dynamically deformed interface: effect of an axial gas flow on the linear stability, *J. Fluid Mech.,* **978,** A27.

Succi, S. & Succi, S., 2018. *The lattice Boltzmann Equation: for Complex States of Flowing Matter,* Oxford University Press.

Tackley, P.J., Ammann, M., Brodholt, J.P., Dobson, D.P. & Valencia, D., 2013. Mantle dynamics in super-earths: Post-perovskite rheology and self-regulation of viscosity, *Icarus,* **225**(1), 50–61.

Tosi, N. et al., 2015a. A community benchmark for viscoplastic thermal convection in a 2-d square box, *Geochem. Geophys. Geosyst.,* **16**(7), 2175–2196.

Tosi, N. et al., 2015b. A community benchmark for viscoplastic thermal convection in a 2-D squared box, *g-cubed,* **16**. doi:10.1002/2015GC005807.

Valencia, D. & O'Connell, R.J., 2009. Convection scaling and subduction on earth and super-earths, *Earth planet. Sci. Lett.,* **286**(3–4), 492–502.

van Hunen, J., van Keken, P.E., Hynes, A., Davies, G.F., Condie, K. & Pease, V., 2008. Tectonics of early earth: Some geodynamic considerations, *When did plate tectonics begin on planet Earth,* pp. 157–171, GeoScienceWorld.

van Keken, P.E., King, S.D., Schmeling, H., Christensen, U.R., Neumeister, D. & Doin, M.-P., 1997. A comparison of methods for the modelling of thermochemical convection, *J. geophys. Res.,* **102,** 22 477–22 495.

van Keken, P.E. et al., 2008. A community benchmark for subduction zone modelling, *Phys. Earth planet. Inter.,* **171**(1–4), 187–197.

van Leer, B., 1979. Towards the ultimate conservative difference scheme. v. a second-order sequel to godunov's method, *J. Comput. Phys.,* **32**(1), 101–136.

Walbecq, A., Samuel, H. & Limare, A., 2024. Fully determined velocity field in a convection experiment with boundary conditions and zero divergence constraints, *Exp. Fluids,* **70**(65). doi:10.1007/s00348-024-03807-y.

Zhong, S., McNamara, A., Tan, E., Moresi, L. & Gurnis, M., 2008. A benchmark study on mantle convection in a 3-d spherical shell using citcoms, *Geochem. Geophys. Geosyst.,* **9**(10). doi:10.1029/2008GC002048.